

Article

# Bifurcation analysis of nonlinear probability model for resting potential and theoretical calculation of human ventricular myocardium elastic modulus

Rui Qu<sup>1,\*</sup>, Xin Xia<sup>2,\*</sup><sup>1</sup> Faculty of Civil Engineering and Mechanics, Jiangsu University, Zhenjiang 212013, China<sup>2</sup> School of Medicine, Jiangsu University, Zhenjiang 212013, China\* **Corresponding authors:** Rui Qu, 1000005286@ujs.edu.cn; Xin Xia, 1000005066@ujs.edu.cn

## CITATION

Qu R, Xia X. Bifurcation analysis of nonlinear probability model for resting potential and theoretical calculation of human ventricular myocardium elastic modulus. *Molecular & Cellular Biomechanics*. 2025; 22(3): 1163. <https://doi.org/10.62617/mcb1163>

## ARTICLE INFO

Received: 18 December 2024

Accepted: 31 December 2024

Available online: 26 February 2025

## COPYRIGHT



Copyright © 2025 by author(s).

*Molecular & Cellular Biomechanics* is published by Sin-Chn Scientific Press Pte. Ltd. This work is licensed under the Creative Commons Attribution (CC BY) license. <https://creativecommons.org/licenses/by/4.0/>

**Abstract:** This paper focuses on the cardiac pulsation model. The first purpose is to explain the generation mechanism of myocardial resting potential from two aspects of nonlinear dynamics and physiology. The second objective is to establish the basic theoretical calculation method for ventricular muscle material parameters such as elastic modulus, Poisson's ratio and shear modulus. The physiological essence of resting potential is ion channel blocking reaction to mismatched ions, which can be described by the probability model of fully misaligned arrangement. The calculation of the elastic modulus of ventricular muscle is based on the stress distribution characteristics at the end of diastole and the modified Laplace' law. The correctness and effectiveness of the misaligned arrangement probability model for resting potential, the modified Laplace's law of cardiac diastole and the three-dimensional pressure equalization theory of cardiac systole are also proved in detail. A theoretical calculation method for ventricular muscle elastic modulus is established relying solely on echocardiography data instead of costly measurement methods such as magnetic resonance imaging (MRI). The reference value for longitudinal elastic modulus of human ventricular muscle was calculated and compared with experimental data of isolated porcine heart. The echocardiography measurement method based on theoretical results may provide potential assistance for the initial screening and diagnosis of cardiogenic diseases as a routine physical examination item.

**Keywords:** nonlinear dynamics; non-smooth; bifurcation; myocardial mechanical behavior; elastic modulus

## 1. Introduction

Myocardium mechanics has been a focus of research for decades because of its significant impact on cardiac physiology [1–5]. Measurement methods of myocardium mechanical properties are of vital importance in diagnosis and treatment of cardiogenic diseases. In recent years, research methods of constructing constitutive equations and deriving theoretical results from the physiological basis of myocardial dynamics have emerged as efficient tools for cardiac function analysis [6–8], which may develop new diagnostic techniques and therapies. In this paper, in order to explain the generation mechanism of myocardial resting potential and calculate the ventricular muscle material parameters, the mathematical model of bioelectricity as well as the mechanical model of myocardium vibration are established respectively based on physiological meanings.

The discharge behaviors of myocardial cells have been widely studied [9–12]. Action potential is mainly caused by the difference in ion concentration inside and outside the cell membrane. However, ion channels have a special function of transporting ions against concentration differences. When the forward and reverse

concentration difference potentials reach equilibrium, the action potential remains a constant, namely the resting potential, which is of vital importance but often ignored in the establishment of bioelectrical models. As an important link between myocardial bioelectric models and cardiac mechanical vibration models, resting potential corresponds to the critical period from end systolic to end diastolic of the ventricle.

In the first part of this paper, we introduce non-smooth terms into common bioelectric models and successfully reproduce the phase portrait of resting potential. Besides, through attractor and vector field analysis [13,14], the differences in action potentials affected by different non-smooth terms are also studied so as to reveal the generation mechanism of resting potential from the perspective of dynamics. In addition, based on the physiological basis of mismatched ions blocked by ion channels, a probability model of fully misaligned arrangement was established to estimate the duration of resting potential, which plays an important role in evaluating the rationality of bioelectric models.

Elastic modulus is an important index to evaluate the health of ventricular muscle. However, due to the lack of noninvasive detection methods, there are only a few limited options for the measurement of myocardial elastic modulus. The common simulation method is to reconstruct the finite element model of the heart employing the data obtained from magnetic resonance imaging (MRI). Its advantage is that the global stress distribution on the myocardium can be observed, while its disadvantages are the high price and long processing time due to the demand for a large amount of data, which makes it unsuitable as a routine physical examination item. The methodology introduced in this paper only needs the cardiac ultrasound data, which means that it has the advantages of low price, high efficiency and suitable for large-scale screening in routine physical examination.

The common experimental method is to measure the elastic modulus of isolated pig heart to estimate the value of human heart [15–17]. Although the experimental measurement steps are not complicated, the shortcomings of this method are also obvious. Firstly, the isolated heart is bound to undergo organic damage to its physiological structure, and the measured value of its elastic modulus cannot accurately estimate the theoretical value of human heart in working state. Different experimental designs and equipment will have a significant impact on the measurement, which leads to a great difference in the data measured by experimental methods in different references [18–22]. Secondly, experimental methods can only obtain estimated value for elastic modulus of human ventricular muscle, thus cannot provide personalized diagnosis for patients.

In the second part of this paper, based on the static model of ventricular muscle at the end of diastole, the theoretical calculation method of the elastic modulus of human ventricular muscle is proposed employing the modified Laplace's law. The limitation of this theoretical method is that it is only applicable to the calculation of radial elastic modulus (myocardium itself is an anisotropic material), while the longitudinal modulus has to be approximated through elasticity theory and linear assumption. However, because only cardiac ultrasound data are needed, it has the advantages of low price, high efficiency and suitable for large-scale screening in routine physical examination.

## 2. Mathematical model of bioelectricity

Hindmarsh and Rose first proposed an neuron model named HR system which can be employed to describe bioelectrical activities of cells. Research shows that a single HR neuron can show different oscillation modes, such as quiescent state, spiking state, bursting and chaos. The equivalent circuit of HR neuron model is shown in **Figure 1**, and the three-dimensional non-autonomous mathematical model of HR neuron system considering external excitation can be expressed as:

$$\begin{cases} \frac{dx}{dt} = y - ax^3 + bx^2 - z + W \\ \frac{dy}{dt} = c - dx^2 - y \\ \frac{dz}{dt} = r[s(x - \chi) - z] \end{cases} \quad (1)$$

The physiological meanings of state variables and parameters in the governing Equation (1) are as follows:

$x$ —membrane potential;  $y$ —quick recovery current;  $z$ —slow-varying adaptive current;

$W = A \sin(\Omega t)$ —external stimulation current;  $\chi$ —resting state adjustment parameter;  $r$ —rate of change related to calcium ion concentration;  $a, b, c, d$ —constant parameters without special physiological significance. It should be noted that due to the extensive theoretical derivation and numerous mathematical symbols involved in this paper, the supplementary theoretical content is provided in Appendix A, while the physical or physiological meanings of the mathematical symbols used are listed in Appendix B.

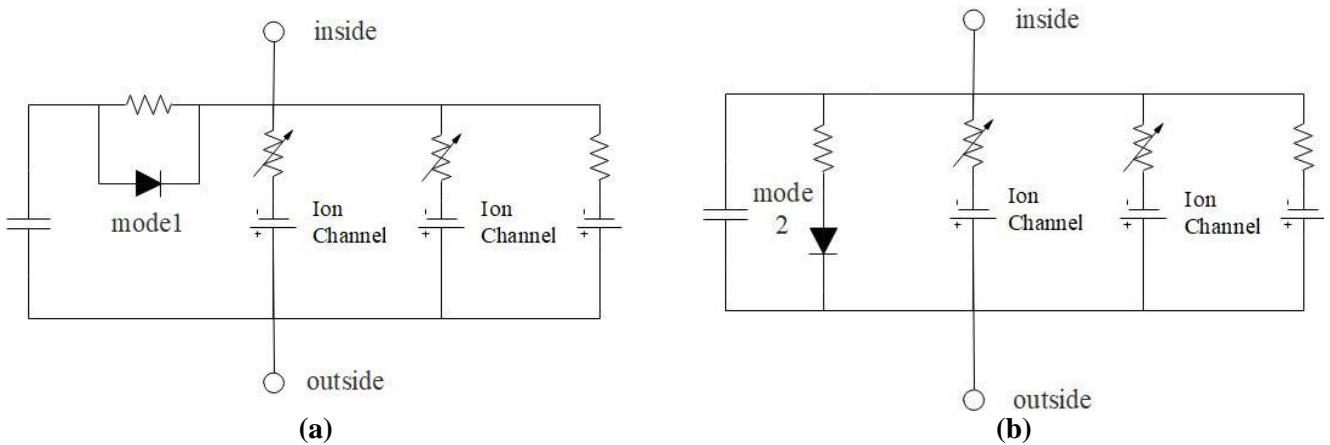


**Figure 1.** Equivalent circuit with non-smooth term. (a) series connection; (b) parallel connection.

### 2.1. Stability and bifurcations of autonomous system

The equilibrium point  $E_0(x, y, z)$  of the system can be uniformly expressed as

$$E_0(x, y, z) = E_0 \left( X_0, c - dX_0^2, s(X_0 - \chi) \right) \quad (2)$$

in which  $X_0$  satisfies the condition

$$aX_0^3 - (b - d)X_0^2 + s(X_0 - \chi) - c = 0 \quad (3)$$

Routh-Hurwitz criterion can be employed to analyze the stability of equilibrium point. The Jacobi matrix of system (1) can be expressed as:

$$J = \begin{bmatrix} -3ax^2 + 2bx & 1 & -1 \\ -2dx & -1 & 0 \\ rs & 0 & -r \end{bmatrix} \quad (4)$$

Therefore, the characteristic equation at the equilibrium point can be formed as:

$$\lambda^3 + k_1\lambda^2 + k_2\lambda + k_3 = 0, \begin{cases} k_1 = 3ax^2 - 2bx + r + 1 \\ k_2 = (3a + 3ar)x^2 + (2d - 2br - 2b)x + rs + r, \\ k_3 = 3arx^2 + (2dr - 2br)x + rs \end{cases} \quad (5)$$

Based on the inference of Routh-Hurwitz stability criterion, the stable conditions of equilibrium points can be formed as

$$k_1 > 0, \begin{vmatrix} k_1 & 1 \\ k_3 & k_2 \end{vmatrix} > 0, k_3(k_1k_2 - k_3) > 0 \quad (6)$$

$$\Downarrow$$

$$k_1 > 0, k_3 > 0, k_1k_2 > k_3$$

Therefore, the stability conditions of the equilibrium point can be expressed as:

$$\begin{cases} 3ax^2 - 2bx + r + 1 > 0 \\ 3ax^2 + (2d - 2b)x + s > 0, r > 0 \\ (3ax^2 - 2bx + r + 1) \times [(3a + 3ar)x^2 + (2d - 2br - 2b)x + rs + r] \\ -[3arx^2 + (2dr - 2br)x + rs] > 0 \end{cases} \quad (7)$$

When condition  $k_3 > 0$  degenerates to  $k_3 = 0$ , the characteristic equation has a zero-root corresponding to the Fold bifurcation conditions:

$$\text{FB: } \begin{cases} 3ax^2 - 2bx + r + 1 > 0 \\ 3arx^2 + (2dr - 2br)x + rs = 0 \Rightarrow x = \frac{b-d \pm \sqrt{(d-b)^2 - 3as}}{3a} \\ (3ax^2 - 2bx + r + 1) \times [(3a + 3ar)x^2 + (2d - 2br - 2b)x + rs + r] \\ -[3arx^2 + (2dr - 2br)x + rs] > 0 \end{cases} \quad (8)$$

When condition  $k_1k_2 > k_3$  degenerates to  $k_1k_2 = k_3$ , a pair of pure imaginary roots appear in the solution of characteristic polynomial (5) indicating the occurrence of Hopf bifurcation. Therefore, the conditions of Hopf bifurcation are as follows:

$$\text{HB: } \begin{cases} 3ax^2 - 2bx + r + 1 > 0 \\ 3ax^2 + (2d - 2b)x + s > 0, r > 0 \\ (3ax^2 - 2bx + r + 1) \times [(3a + 3ar)x^2 + (2d - 2br - 2b)x + rs + r] \\ = [3arx^2 + (2dr - 2br)x + rs] \end{cases} \quad (9)$$

From the calculation results, it can be seen that the analytical expression of the bifurcation point is complicated. For simplicity, slow-varying adaptive current  $z$  can be ignored when the external excitation amplitude is much larger. Therefore, HR neuron system (1) can be further simplified to a two-dimensional degenerate system

$$\begin{cases} \frac{dx}{dt} = y - ax^3 + bx^2 + W \\ \frac{dy}{dt} = c - dx^2 - y \end{cases} \quad (10)$$

The equilibrium point  $E_0(x, y)$  of the system can be uniformly expressed as

$$E_0(x, y) = E_0(X_0, c - dX_0^2) \quad (11)$$

in which  $X_0$  satisfies the condition

$$aX_0^3 - (b - d)X_0^2 - c - w = 0 \quad (12)$$

The Jacobi matrix of system (10) can be expressed as

$$J = \begin{bmatrix} -3ax^2 + 2bx & 1 \\ -2dx & -1 \end{bmatrix} \quad (13)$$

the corresponding characteristic equation at the equilibrium point can be formed as

$$\lambda^2 + (3ax^2 - 2bx + 1)\lambda + 3ax^2 + 2(d - b)x = 0 \quad (14)$$

Therefore, the stability conditions of the equilibrium point can be expressed as

$$\begin{cases} 3ax^2 - 2bx + 1 > 0 \\ 3ax^2 + 2(d - b)x > 0 \end{cases} \quad (15)$$

The bifurcation condition corresponding to a characteristic polynomial having zero solutions or pure imaginary roots can be respectively expressed as:

$$\text{FB: } \begin{cases} 3ax^2 - 2bx + 1 > 0, \\ 3ax^2 + 2(d - b)x = 0. \end{cases} \Rightarrow \begin{cases} x = \frac{2(b-d)}{3a}, 0 \\ 2dx < 1 \end{cases} \quad (16)$$

and

$$\text{HB: } \begin{cases} 3ax^2 - 2bx + 1 = 0, \\ 3ax^2 + 2(d - b)x > 0. \end{cases} \Rightarrow \begin{cases} x = \frac{b \pm \sqrt{b^2 - 3a}}{3a} \\ 2dx > 1 \end{cases} \quad (17)$$

It should be pointed out that the frequency of stable limit cycle generated by Hopf bifurcation is the natural frequency of system, which can be calculated by

$$\Omega_0 = \sqrt{3ax^2 + 2(d - b)} \quad (18)$$

## 2.2. Simulations with non-smooth terms

The resting potential (sliding trajectory) has typical non-smooth characteristics, so the non-smooth term is bound to be introduced for its simulation. From the perspective of equivalent circuit shown in **Figure 1**, non-smooth circuit elements can function as a bidirectional diode to affect the potential of the system through series or parallel connections, which indicates that feedback caused by non-smooth terms can exist in various forms.

The threshold feedback condition can be univariate or multivariable while the feedback term can be a constant term, a linear term, or a nonlinear term. In order to reveal the influence of non-smooth terms on the dynamic behaviors of the system, it is necessary to analyze the smooth case first.

The dynamics of smooth systems under threshold-free control described by **Figure 2** are relatively simple. It can be seen from **Figure 1a,b** that the trajectory starts from and moves almost strictly along the stable branch  $E_{1-}$  before the Fold bifurcation. Once the trajectory reaches the bifurcation point  $FB_2 = (3, -2)$ , it will jump to the focal stable equilibrium branch  $E_{3+}$  due to Fold bifurcation. After convergence to  $E_{3+}$ , the trajectory moves along the branch  $E_{3+}$ ,  $E_{2+}$  and  $E_{1+}$  before jumping phenomenon caused by Fold bifurcation point  $FB_1 = (-1, 0)$ .

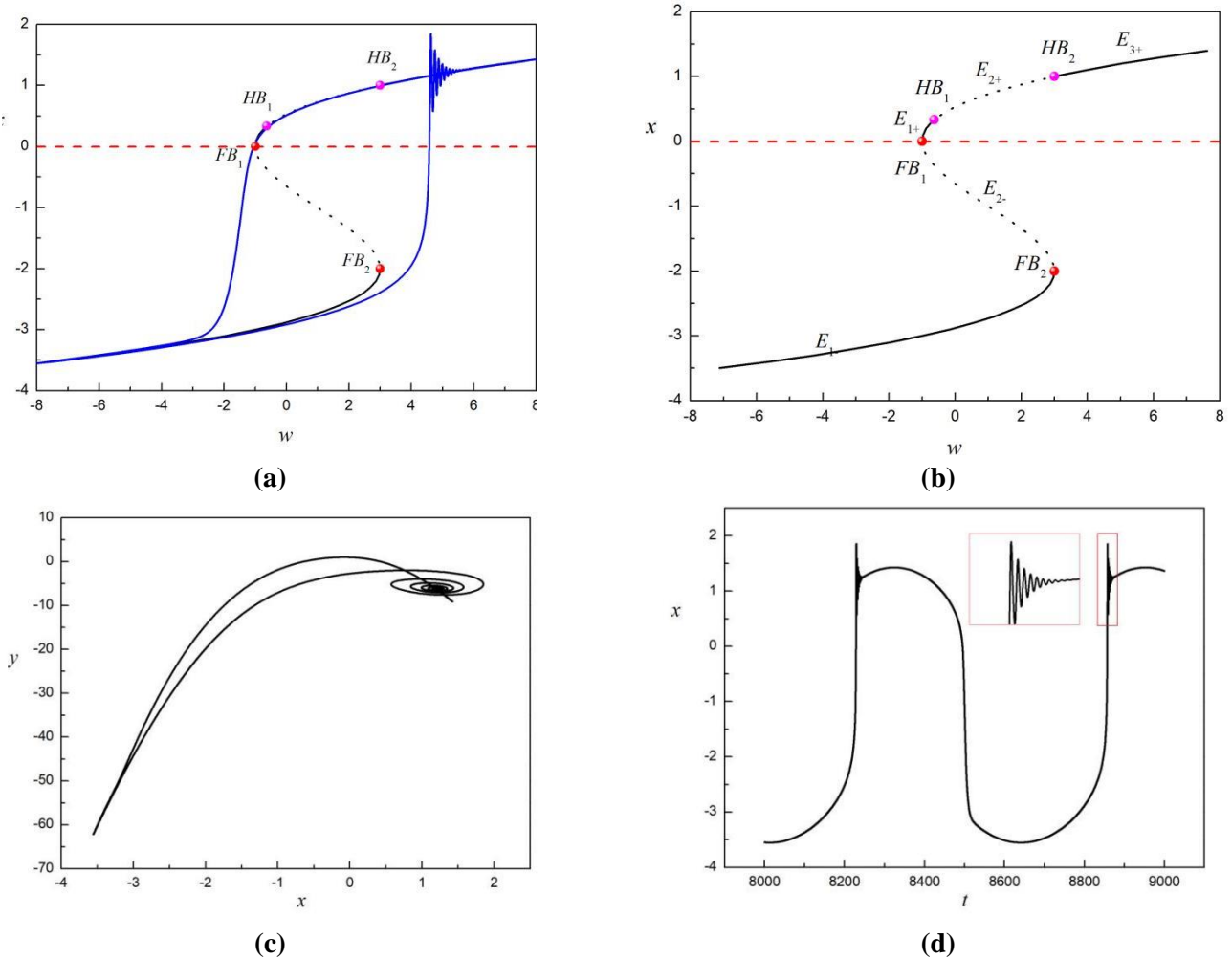


**Figure 2.** Smooth system with  $a = 1.0, b = 2.0, c = 1.0, d = 5.0, A = 8.0, \Omega = 0.01$ . **(a)** transformed phase portrait; **(b)** equilibrium branches; **(c)** phase portrait; **(d)** time history.

There are two special dynamic behaviors in the oscillation period that need to be supplemented. The first one is the delay effect between two bifurcation points  $HB_1 = (-\frac{17}{27}, \frac{1}{3})$  and  $HB_2 = (3, 1)$ . To be specific, the trajectory moves along the unstable branch  $HB_2$  instead of being attracted by the limit circle caused by Hopf bifurcation. The reason for this phenomenon is that the divergence speed of trajectory in the neighborhood of unstable equilibrium point is less than the changing velocity of equilibrium point due to external excitation. The second phenomenon worth noting is that the trajectory fails to move strictly along the stable branch  $E_{1-}$  before reaching the bifurcation point  $FB_2$ . The reason for the trajectory deviating from the stable

branch is that the external excitation is in the form of a sine function, which has a higher rate of change near zero. In other words, when the external excitation is close to zero, the convergence rate of the trajectory toward the stable equilibrium point is less than the change rate of the equilibrium point. To further verify this conclusion, the dynamic behaviors when the external excitation frequency  $\Omega$  is reduced to 0.001 are shown in **Figure 3**.

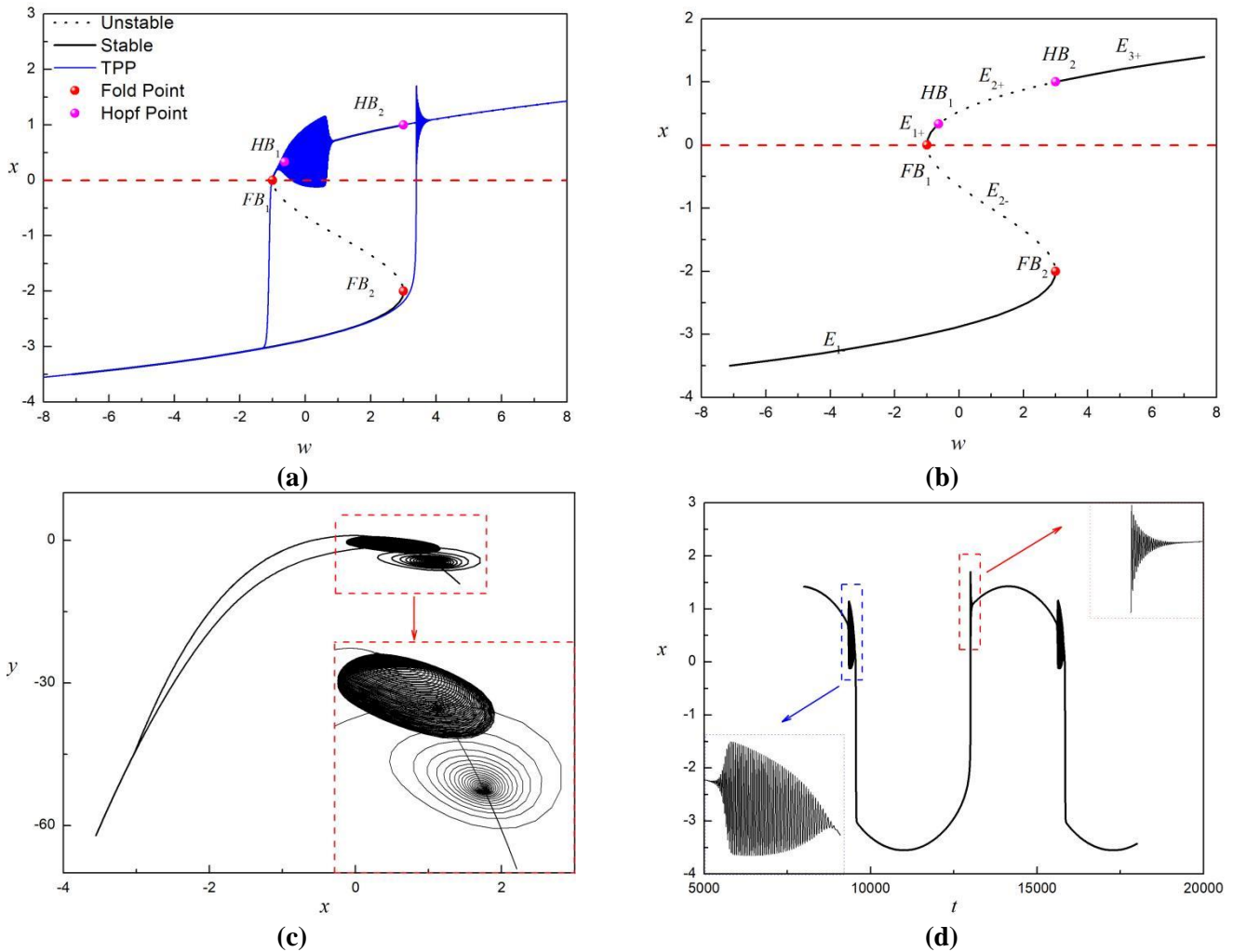


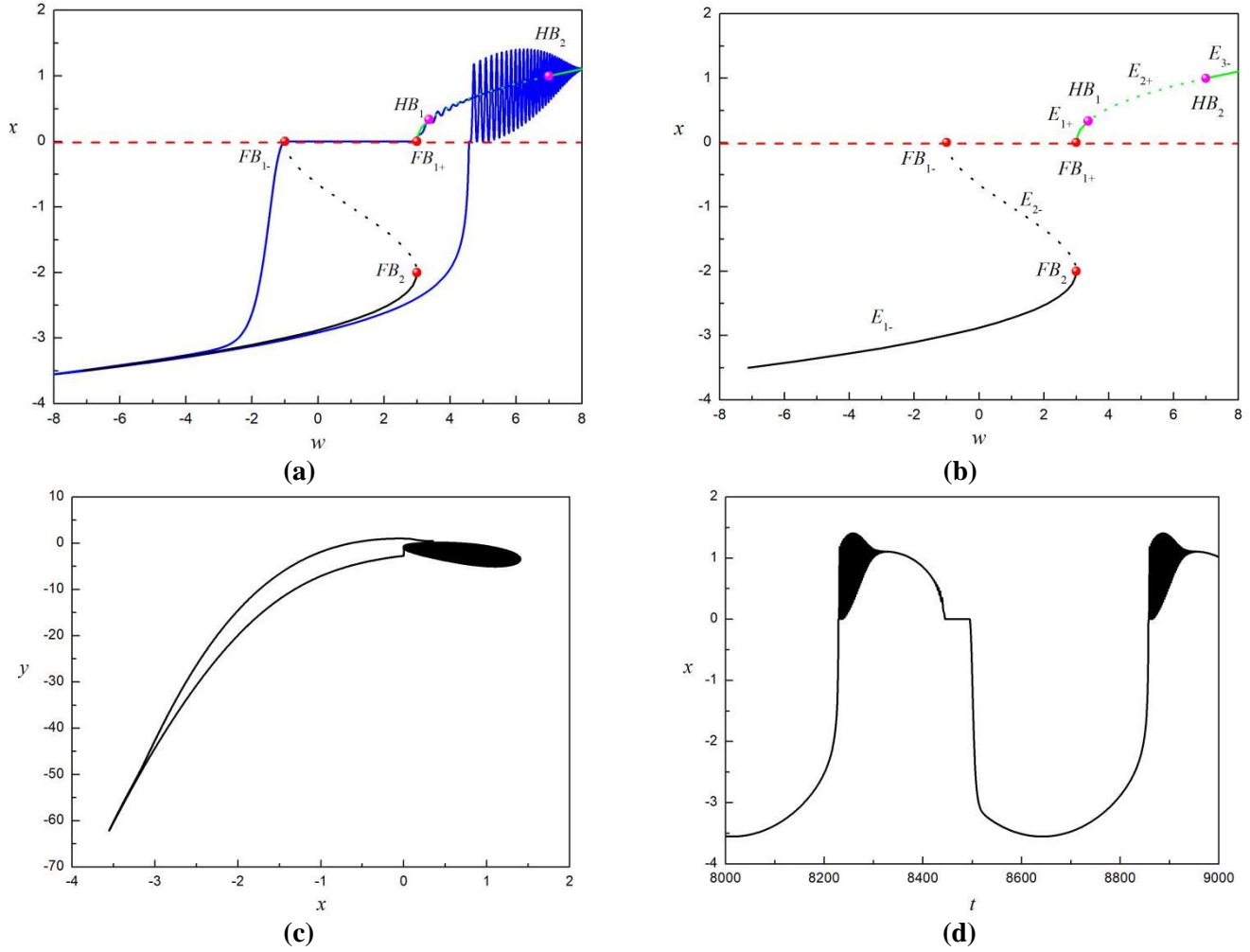
**Figure 3.** Smooth system with  $\Omega = 0.001$ . **(a)** transformed phase portrait; **(b)** equilibrium branches; **(c)** phase portrait; **(d)** time history.

Comparing **Figures 2a** and **3a**, it can be concluded that the topology of the trajectory may change under different external excitation frequencies although it is affected by the same equilibrium branch. To be specific, relatively lower external excitation frequency results in a smaller equilibrium point migration speed, thereby eliminating the delay effect and trajectory deviation phenomenon.

It is not difficult to find that the governing equation of the HR system is smooth, so it is impossible to simulate the resting potential of the heart. Therefore, the feedback term  $\Delta I$  is introduced as a non-smooth term to modify smooth HR systems:

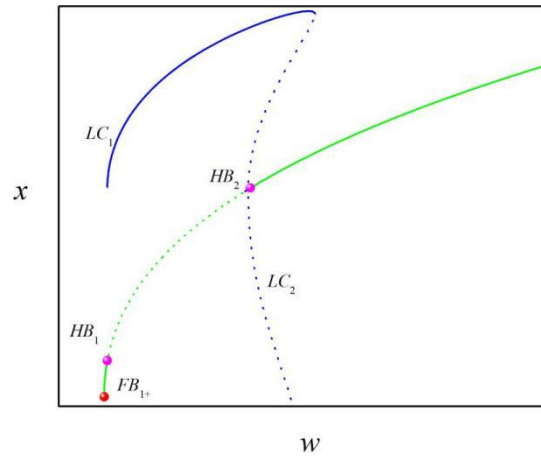
$$x > 0: \begin{cases} \frac{dx}{dt} = y - ax^3 + bx^2 + W + \Delta I \\ \frac{dy}{dt} = c - dx^2 - y \end{cases}, x < 0: \begin{cases} \frac{dx}{dt} = y - ax^3 + bx^2 + W - \Delta I \\ \frac{dy}{dt} = c - dx^2 - y \end{cases} \quad (19)$$

The dynamic behaviors of the modified non smooth HR system are shown in **Figure 4**.



**Figure 4.** Non-smooth system with  $\Delta I = -4.0$ . (a) transformed phase portrait; (b) equilibrium branches; (c) phase portrait; (d) time history.

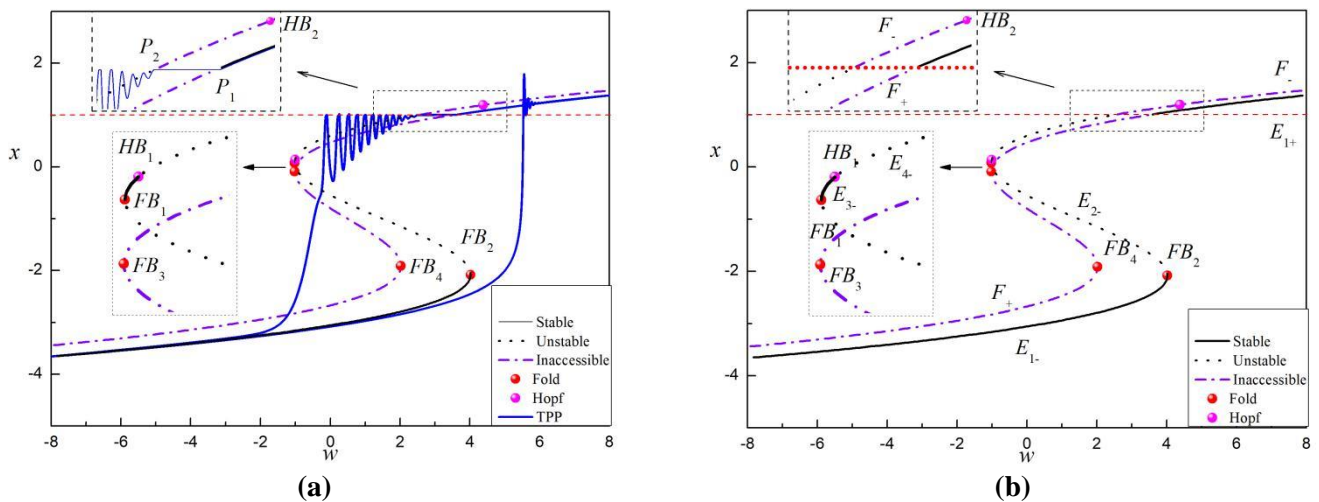
It can be seen from **Figure 4a,b** that the trajectory starts from and moves almost strictly along the stable branch  $E_{1-}$  until it reaches the Fold bifurcation point  $FB_2 = (3, -2)$ . Then, the trajectory jumps towards and directly traverses the non-smooth boundary  $x = 0$ . After that, the trajectory oscillates around the stable limit cycle  $LC_1$  generated by the Hopf bifurcation point  $HB_1 = (3.3704, \frac{1}{3})$ . The collision between unstable limit cycle  $LC_2$  bifurcated from  $HB_2 = (7, 1)$  and stable limit cycle  $LC_1$  results in their disappearance and leads to the convergence of the trajectory towards the stable focal equilibrium branch  $E_{3+}$ . This process is named LPC bifurcation, and its topological structure is shown in **Figure 5**.



**Figure 5.** The topological structure of LPC bifurcation.

After the limit point bifurcation of cycles (LPC), the trajectory returns to the non-smooth boundary along the branches  $E_{2+}$  and  $E_{3+}$  at the Fold bifurcation point  $FB_{1+}$ . On the non-smooth boundary, the trajectory slides from  $FB_{1+}$  to  $FB_{1-}$  and finally converges to the stable branch  $E_{1-}$ . From the perspective of geometric properties, there are three types of motion when the trajectory and non smooth interface come into contact, namely sliding, traversing, and jumping. Employing the vector field analysis method, the mechanism of motion patterns can be well explained. To be specific, sliding motion may occur when the inner product of the vector fields on both sides of the non-smooth boundary is negative (points towards the interface at the same time). On the contrary, if the inner product of the vector fields on both sides is positive, the trajectory will directly traverse the interface. Jumping phenomenon is a critical situation for sliding and traversing (one side vector field is zero).

Although vector field theory can directly explain the local non-smooth dynamics of trajectory, it fails to solve the global non-smooth bifurcation problems of the system. In order to further elucidate the mechanism of resting potential from a dynamical perspective, the attractor structure has to be considered. In fact, the threshold control term may be a function of the state variable instead of remaining a constant. To simulate this situation, the dynamic behaviors of the non-smooth system with linear feedback term  $\Delta I = -0.5x$  are shown in **Figure 6**.



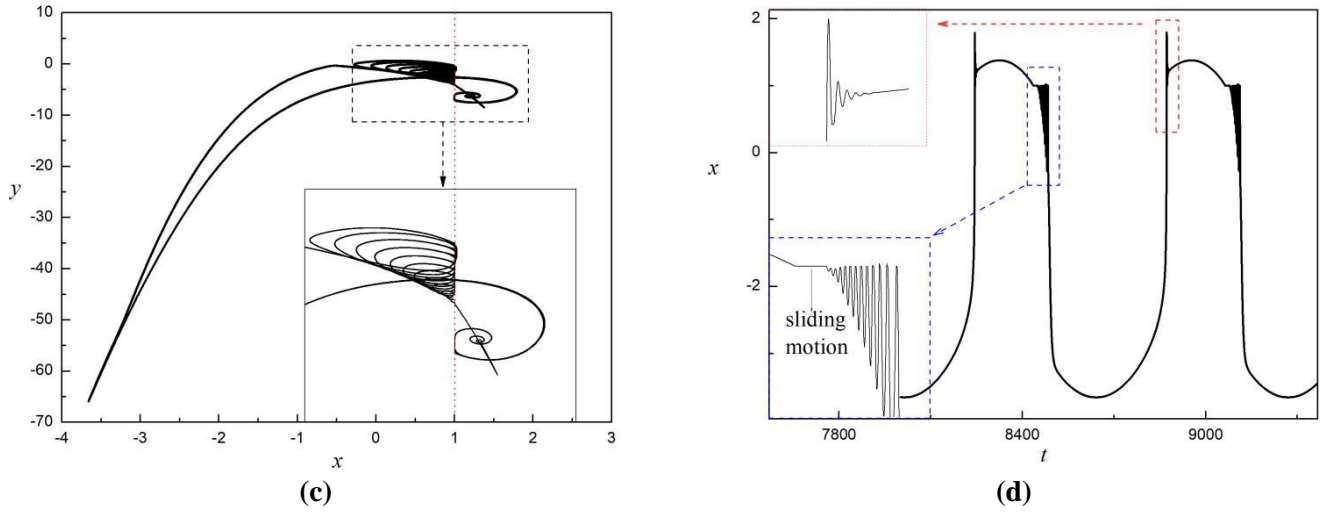


**Figure 6.** Non-smooth system with  $\Delta I = -0.5x$ . (a) transformed phase portrait; (b) equilibrium branches; (c) phase portrait; (d) time history.

In this case, two subsystems can be represented as:

$$x > 1: \begin{cases} \frac{dx}{dt} = y - ax^3 + bx^2 + W + kx \\ \frac{dy}{dt} = c - dx^2 - y \end{cases}, x < 1: \begin{cases} \frac{dx}{dt} = y - ax^3 + bx^2 + W - kx \\ \frac{dy}{dt} = c - dx^2 - y \end{cases} \quad (20)$$

Equilibrium condition (12) turns into:

$$aX_0^3 - (b-d)X_0^2 - kX_0 - c - W = 0 \quad (21)$$

Jacobian matrix becomes:

$$J = \begin{bmatrix} -3ax^2 + 2bx + k & 1 \\ -2dx & -1 \end{bmatrix} \quad (22)$$

The characteristic Equation (14) changes into:

$$\lambda^2 + (3ax^2 - 2bx + 1 - k)\lambda + 3ax^2 + 2(d-b)x - k \quad (23)$$

Therefore, two types of codimension-one bifurcation conditions can be expressed as:

$$\text{FB: } \begin{cases} 3ax^2 - 2bx + 1 - k > 0, \\ 3ax^2 + 2(d-b)x - k = 0, \end{cases} \Rightarrow \begin{cases} x = \frac{-(d-b) \pm \sqrt{(d-b)^2 + 3ak}}{3a} \\ 2dx < 1 \end{cases} \quad (24)$$

and

$$\text{HB: } \begin{cases} 3ax^2 - 2bx + 1 - k = 0, \\ 3ax^2 + 2(d-b)x - k > 0. \end{cases} \Rightarrow \begin{cases} x = \frac{b \pm \sqrt{b^2 + 3a(k-1)}}{3a} \\ 2dx > 1 \end{cases} \quad (25)$$

The coordinates of the bifurcation point in the transformed phase portrait can be calculated as:

$$\begin{cases} FB_1 = (-1.0203, 0.0801) \\ FB_2 = (4.0203, -2.0801) \\ FB_3 = (-1.0214, -0.0871) \\ FB_4 = (2.0215, -1.9129) \\ HB_1 = (-1.0086, 0.1396) \\ HB_2 = (4.3790, 1.1937) \end{cases} \quad (26)$$

In order to analyze the attractor structure, the functions of inaccessible equilibrium branches are also ought to be considered. It should be pointed out that although the inaccessible equilibrium branches are not located within the domain of the corresponding subsystem, they can still affect the vector field structure within the domain. In other words, false equilibrium points can also control the dynamic behaviors of trajectory just like true equilibrium points.

Specifically, the trajectory moves along the stable true branch  $E_{1-}$  then jumps to the true stable branch  $E_{1+}$  due to the Fold bifurcation point  $FB_2 = (4.0203, -2.0801)$ . After converging to the stable focal branch  $E_{1+}$ , the trajectory returns to the non-smooth boundary at point  $P_1$ . The sliding motion occurred between point  $P_1$  and  $P_2$  can be explained by the alternating attraction of false stable equilibrium points in different phase regions. In the sliding interval, if the trajectory is located above the non-smooth boundary ( $x > 1$ ), it will be attracted by the stable false branch  $F_+$ . Meanwhile, if the trajectory is located below the non-smooth boundary, it will be attracted by the stable false branch  $F_-$  ( $x < 1$ ). The alternating attraction of false stable branches leads to a tendency for the trajectory to approach the boundary in its vicinity, which is the essential mechanism of sliding motion from the perspective of attractor structure. In order to further verify this conclusion, the threshold feedback parameters can be appropriately changed to observe the dynamic behavior of the system with different attractor structures as shown in **Figure 7**.

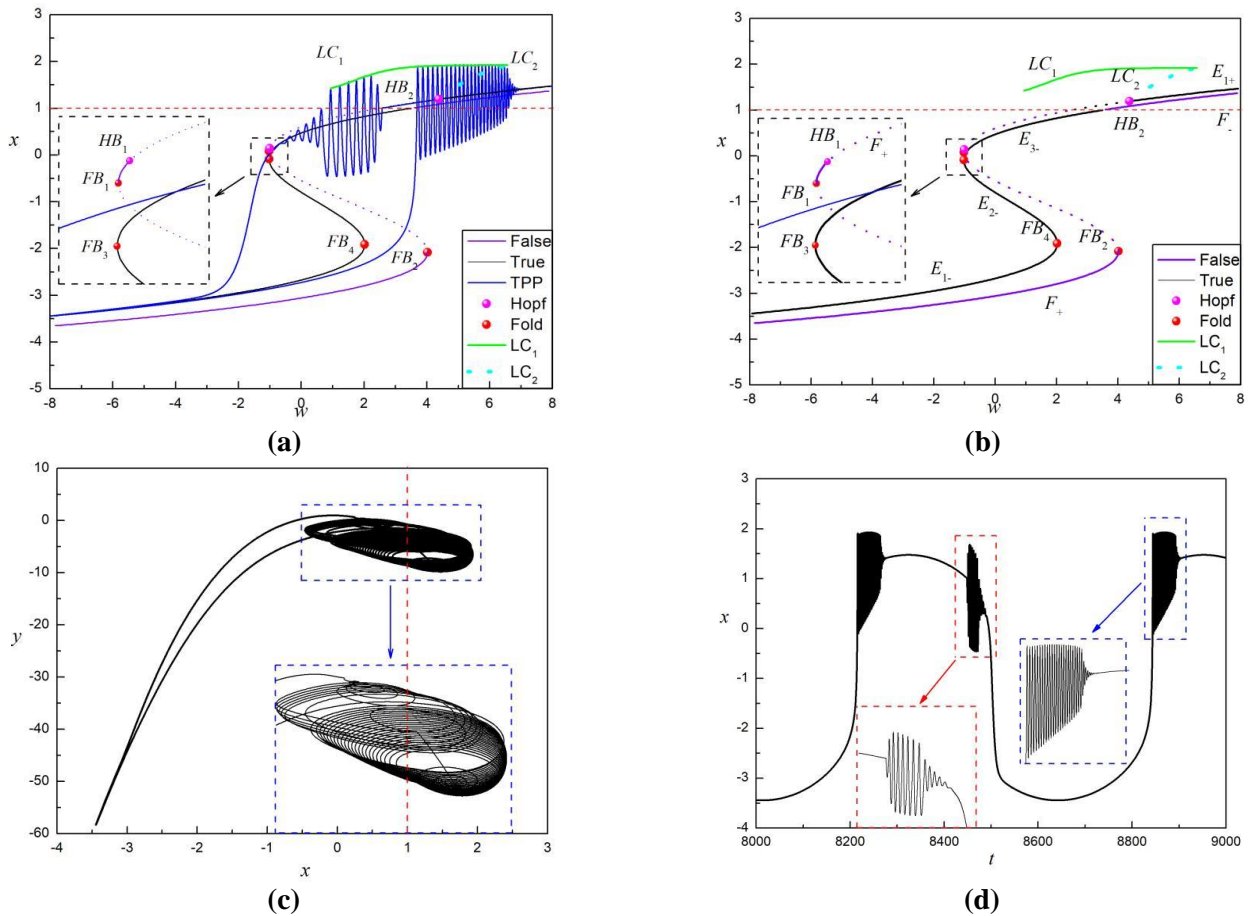


**Figure 7.** Non-smooth system with  $I = +0.5x$ . **(a)** transformed phase portrait; **(b)** equilibrium branches; **(c)** phase portrait; **(d)** time history.

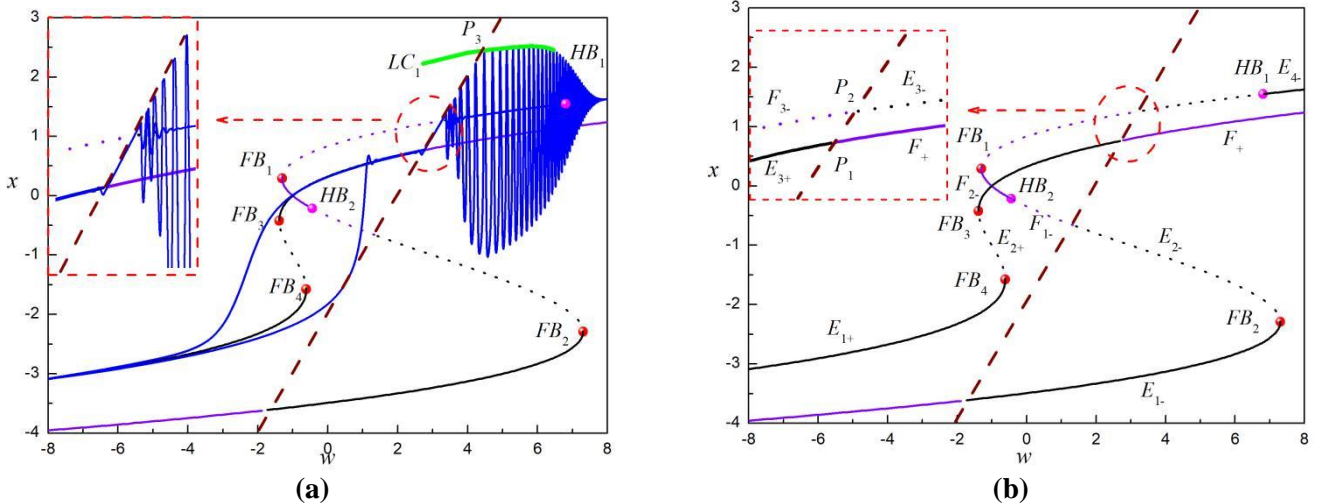
It can be seen from **Figure 7a** that a slight change in the threshold feedback term may cause a drastic change in the oscillation structure of the system even with the same equilibrium branches of **Figure 6a**. Specifically, after moving along the stable branch  $E_{1-}$  and bifurcating due to the Fold point  $FB_4$ , the trajectory traverses the non-smooth boundary due to the attraction of the stable false branch  $F_-$ . Once it locates above the boundary, it will be attracted by the stable limit circle  $LC_1$  generated by the Hopf bifurcation point  $HB_1$ . Under the alternating attraction of  $F_-$  and  $LC_1$ , the trajectory crosses the boundary repeatedly until  $LC_1$  and the unstable limit circle  $LC_2$  bifurcated from  $HB_2$  coincide and vanish together due to the  $LPC$  bifurcation. Afterwards, the trajectory converges to the stable focal branch  $E_{1+}$  and returns to the boundary. Then, it crosses the boundary repeatedly resulted from the alternating attraction of  $LC_1$  and stable branch  $E_{3-}$ . Finally, it jumps back to  $E_{1-}$  due to the Fold bifurcation  $FB_1$ .

The threshold control conditions in all the above cases only involve a single state variable, while in reality, the threshold conditions may be constrained by multiple state variables, which should also be considered. For the sake of simplicity and intuitiveness, we assume the critical condition for threshold control to be the following linear relationship:

$$\begin{cases} x = W - 2.0, \\ \Delta I = -2.0x. \end{cases} \quad (27)$$

The simulation results for this case are shown in **Figure 8**. The coordinates of the bifurcation point in the transformed phase portrait can be calculated as:

$$\begin{cases} FB_1 = (-1.3033, 0.2910), \\ FB_2 = (7.3033, -2.2901), \\ FB_3 = (-1.3849, -0.4226), \\ FB_4 = (-0.6151, -1.5774), \\ HB_1 = (6.8108, 1.5486), \\ HB_2 = (-0.4405, -0.2153). \end{cases} \quad (28)$$



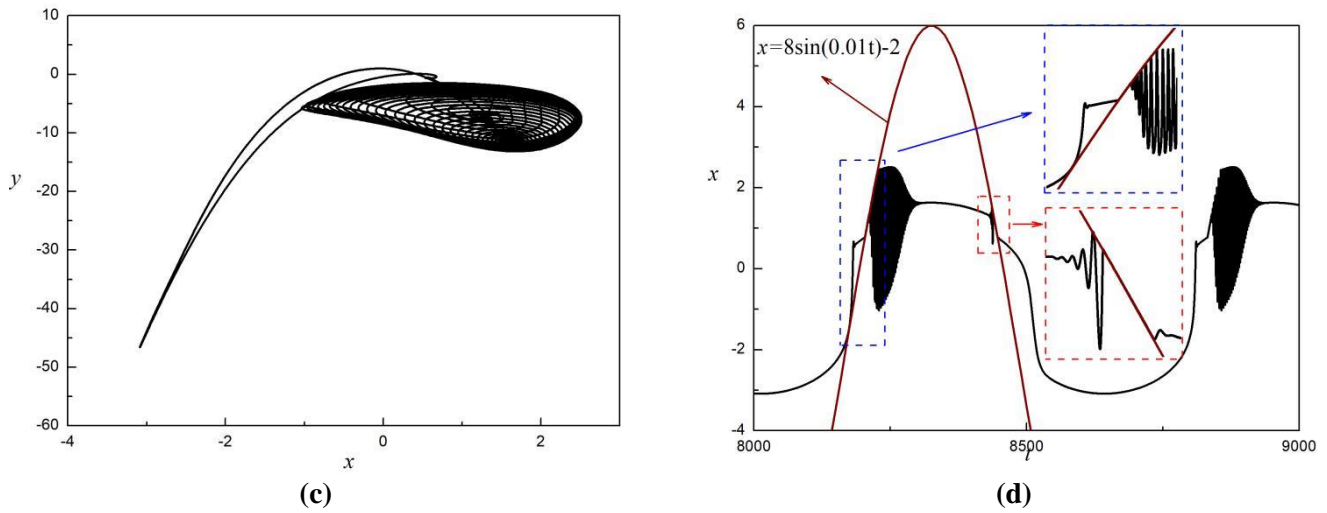


**Figure 8.** Non-smooth system with linear threshold control conditions. (a) transformed phase portrait; (b) equilibrium branches; (c) phase portrait; (d) time history.

Intriguingly, the non-smooth boundary in the transformed phase portrait is a slanted line rather than a horizontal line. Therefore, it should be noted that when analyzing non-smooth phenomena with the vector field structure theory, one should use the normal component of the vector field instead of itself near the non-smooth boundary. By employing attractor structure analysis, this issue can be circumvented.

To be specific, it can be clearly seen from **Figure 8a,b** that the trajectory moves along the stable branch  $E_{1+}$  and jumps to the stable focal branch  $E_{3+}$  due to the Fold bifurcation  $FB_4$ . Once the trajectory traverses the non-smooth boundary at point  $P_1$ , the control branch will switch from  $E_{3+}$  to  $F_{3-}$ . Then, in response to the attraction of the limit cycle  $LC_1$  generated from the Hopf bifurcation, the trajectory is inclined to return to the boundary. In short, the alternating attraction of  $LC_1$  and  $E_{3+}$  leads to the sliding motion between points  $P_1$  and  $P_2$ . After the intersection point  $P_3$  of  $LC_1$  and non-smooth boundary, the subsystem will no longer switch, and the trajectory is completely controlled by the true equilibrium branch  $E_{3-}$ , ultimately converging to stable focal branch  $E_{4-}$ .

The dynamic behaviors of the other half of the oscillation cycle are relatively simple. The trajectory starts from  $E_{4-}$  and moves along the unstable branch  $E_{3-}$  due to the bifurcation delay effect. Based on previous analysis, it can be concluded that the sliding interval of the trajectory in this case is from point  $P_1$  to point  $P_3$ . Therefore, the trajectory slides to  $P_1$  and moves along  $E_{3+}$  before jumping to  $E_{1+}$  caused by Fold bifurcation  $FB_3$ . The sliding motion generated by threshold control conditions involving multiple state variables can also be reflected as the envelope of a sine function on the time history **Figure 8d**.

### 3. The biological and mathematical significance of sliding time

#### 3.1. Probability model

The mathematical meaning of the proportion of sliding time to the entire system cycle can be understood as the probability of a resting potential occurring within a single bursting discharge cycle. The generation of resting potential can be simplified

as the following probability model shown in **Figure 9**. Ion channels are selective to different ions, which means that one ion can only pass through well-matched ion channel. Therefore, the appearance of resting potential implies a completely misaligned arrangement of different ion channels. The core issue for this simplified probability problem is the analytical expression for the total number of completely misaligned permutations  $a_n$  of  $n$  elements.

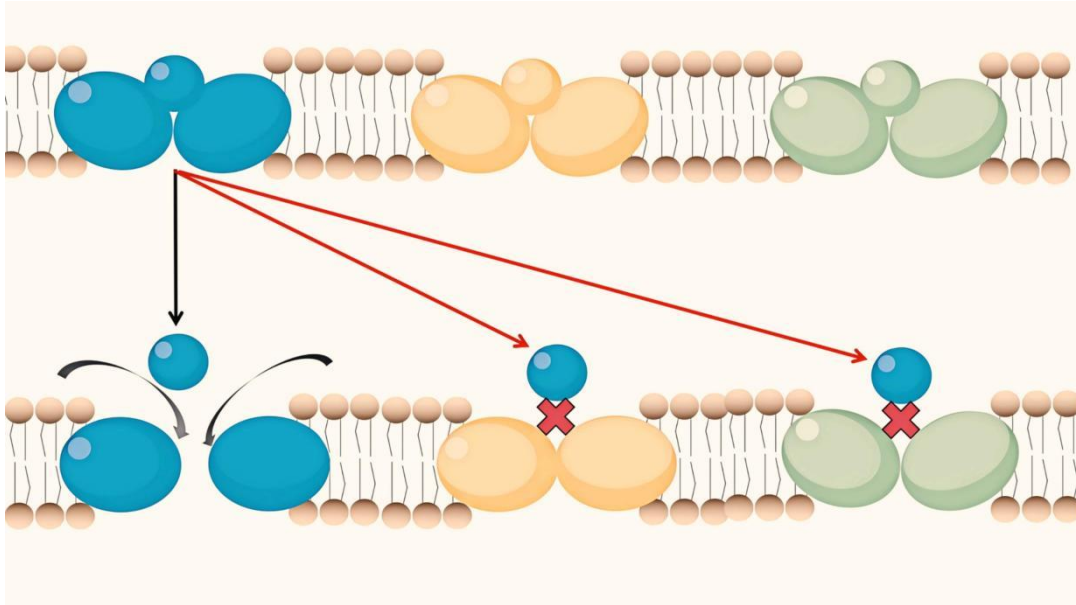


**Figure 9.** Probability model of resting potential.

The core issue of the counting principle is classification. The classification of completely misaligned arrangements can be based on the number of elements participating in the closed-loop. Starting from the first element  $A$ , the second step is to select the next element. Assuming that the second step forms a second-order closed-loop shown in **Figure 10**, the total number of classifications in this case can be expressed as:

$$(n - 1) \times a_{n-2} \quad (29)$$

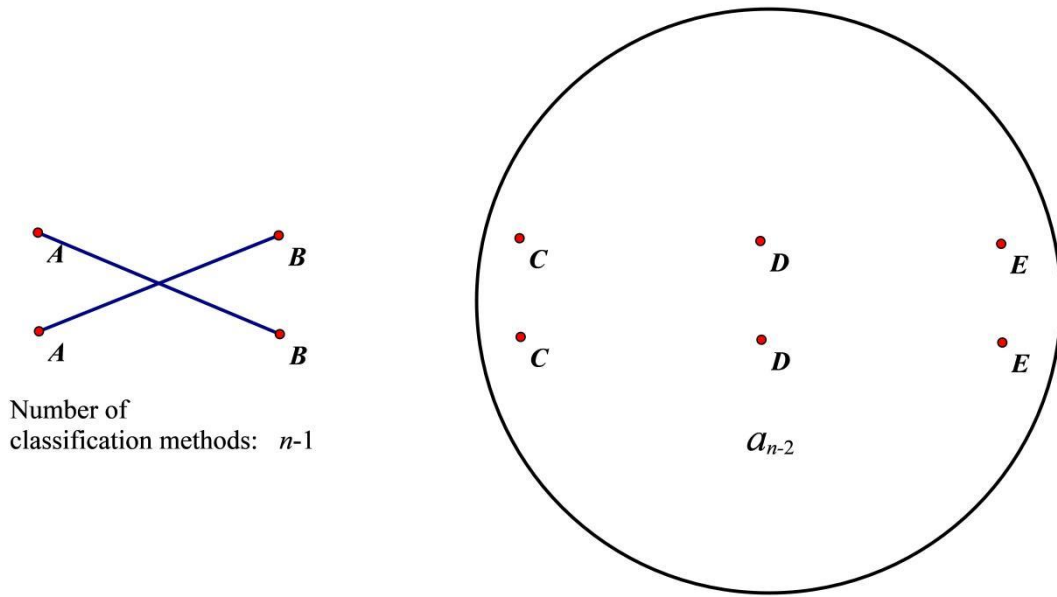


**Figure 10.** The second-order closed-loop fully misaligned arrangement.

Assuming that the third step forms a third-order closed-loop shown in **Figure 11**, the total number of classifications in this case can be expressed as  $(n - 1) \times (n - 2) \times a_{n-3}$ .

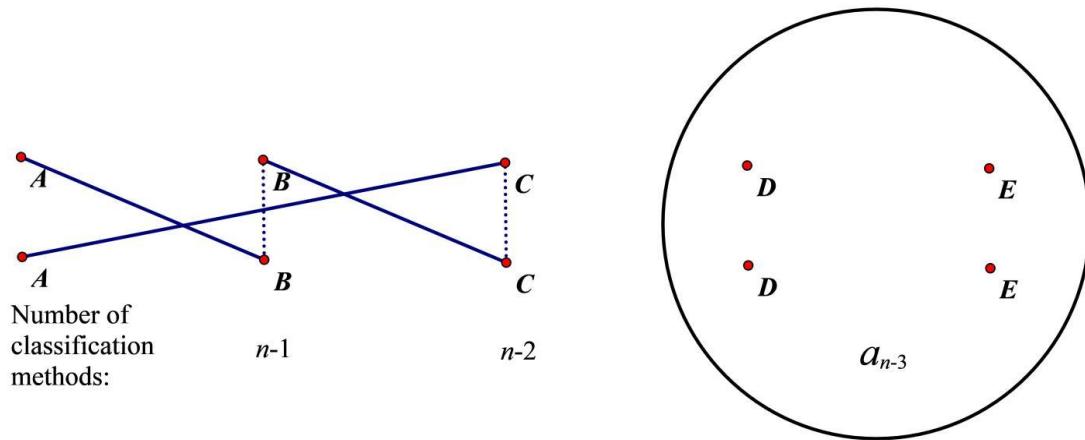


**Figure 11.** The third-order closed-loop fully misaligned arrangement.

By analogy, the total number of classifications which forms an  $n$ th-order closed-loop in step  $n$  can be solved sequentially. Therefore, when  $n \geq 4$ , the total number of completely misaligned permutations can be expressed as:

$$\begin{aligned}
 a_n &= (n - 1) \times a_{n-2} \\
 &+ (n - 1) \times (n - 2) \times a_{n-3} \\
 &+ \dots \\
 &+ (n - 1) \times (n - 2) \dots \times 3 \times a_2 \\
 &+ (n - 1)!.
 \end{aligned}
 \tag{30}$$

Thus,

$$\begin{aligned}
 a_{n-1} &= (n-2) \times a_{n-3} \\
 &+ (n-2) \times (n-3) \times a_{n-4} \\
 &+ \dots \\
 &+ (n-2) \times (n-3) \dots \times 3 \times a_2 \\
 &+ (n-2)!.
 \end{aligned} \tag{31}$$

Multiplying both sides by  $n-1$  to equation (31), it can be obtained that

$$\begin{aligned}
 (n-1)a_{n-1} &= (n-1) \times (n-2) \times a_{n-3} \\
 &+ (n-1) \times (n-2) \times (n-3) \times a_{n-4} \\
 &+ \dots \\
 &+ (n-1) \times (n-2) \times (n-3) \dots \times 3 \times a_2 \\
 &+ (n-1)! \\
 &= a_n - (n-1) \times a_{n-2}.
 \end{aligned} \tag{32}$$

Combined with initial value validation

$$a_1 = 0, a_2 = 1, a_3 = 2 \tag{33}$$

the following recursive relationship can be obtained:

$$a_n = (n-1)(a_{n-1} + a_{n-2}), n \geq 3 \tag{34}$$

Transforming the recursive formula, it can be concluded that

$$a_n = (n-1)(a_{n-1} + a_{n-2}) \Rightarrow a_n - na_{n-1} = -[a_{n-1} - (n-1)a_{n-2}] \tag{35}$$

Observing the correlation between two sides of the above equation (35), it can be assumed that

$$b_n = a_n - na_{n-1} \Rightarrow b_{n-1} = a_{n-1} - (n-1)a_{n-2}. \tag{36}$$

Therefore,

$$\frac{b_n}{b_{n-1}} = -1 \Rightarrow b_n = (-1)^n, n \geq 3 \tag{37}$$

which indicates that

$$a_n - na_{n-1} = (-1)^n \Rightarrow a_n = na_{n-1} + (-1)^n, n \geq 2. \tag{38}$$

After iteration, it can be organized into

$$\begin{aligned}
 a_n &= (-1)^n + (-1)^{n-1} \times n + (-1)^{n-2} \times n \times (n-1) + \dots + (-1)^0 \times n! \\
 &= n! + (-1)^1 \times n \times (n-1) \times \dots \times 2 + (-1)^2 \times n \times (n-1) \times \dots \times 3 + \dots + (-1)^n \\
 &= n! + (-1)^1 \times \frac{n!}{1!} + (-1)^2 \times \frac{n!}{2!} + \dots + (-1)^{n-1} \times \frac{n!}{(n-1)!} + (-1)^n \times \frac{n!}{n!} \\
 &= n! \left[ 1 + (-1)^1 \times \frac{1}{1!} + (-1)^2 \times \frac{1}{2!} + \dots + (-1)^n \times \frac{1}{n!} \right].
 \end{aligned} \tag{39}$$

Assuming that

$$c_n = [1 + (-1)^1 \times \frac{1}{1!} + (-1)^2 \cdot \frac{1}{2!} + \dots + (-1)^n \times \frac{1}{n!}] \quad (40)$$

combined with equation (39), it can be observed that

$$a_n = n! \times c_n \quad (41)$$

It should be noted that the expression of  $c_n$  and the series expansion of  $f(x) = e^x$  have a high degree of similarity. In specific,

$$e^x = x + \frac{x^2}{2!} + \dots + \frac{x^n}{n!} + \dots \quad (42)$$

Besides, the point corresponding to  $x = -1$  is within the convergence domain of its power series. Therefore,

$$e^{-1} = -1 + \frac{(-1)^2}{2!} + \dots + \frac{(-1)^n}{n!} + \dots = c_n + \frac{(-1)^{n+1}}{(n+1)!} + \frac{(-1)^{n+2}}{(n+2)!} + \dots \quad (43)$$

Comparing Equation (43) with Equation (41), one may find that

$$\frac{n!}{e} \approx a_n \quad (44)$$

In another words, the expression of  $\frac{n!}{e}$  is appropriate for the approximate calculation of  $a_n$ . Based on this, error estimation is necessary. It can be proved that

$$\left| \frac{n!}{e} - a_n \right| < 1 \quad (45)$$

In specific, the difference between  $\frac{n!}{e}$  and  $a_n$  can be expressed as

$$\begin{aligned} d_n &= n! \times e^{-1} - n! \times c_n = n! \left[ \frac{(-1)^{n+1}}{(n+1)!} + \frac{(-1)^{n+2}}{(n+2)!} + \dots \right] \\ &= \frac{(-1)^{n+1}}{(n+1)} + \frac{(-1)^{n+2}}{(n+2)(n+1)} + \frac{(-1)^{n+3}}{(n+3)(n+2)(n+1)} + \dots \end{aligned} \quad (46)$$

It can be found that If  $n$  is an odd number, the sum of the first and second terms in the above equation is greater than zero, and the sum of the adjacent two terms thereafter is all positive. Therefore,

$$0 < d_n \quad (47)$$

Besides, the sum of the second and third terms is less than zero, and the sum of the adjacent two terms thereafter is all negative. Therefore,

$$d_n < \frac{1}{n+1} < 1 \quad (48)$$

In general,

$$0 < d_n < \frac{1}{n+1} < 1 \quad (49)$$

If  $n$  is an even number, the following conclusion can be proved by similar methods:

$$-1 < \frac{-1}{n+1} < d_n < 0 \quad (50)$$

In summary,

$$-1 < d_n < 1 \Rightarrow |d_n| < 1, \text{ q.e.d.} \quad (51)$$

In addition, it can be also concluded from the above proof process that if  $n$  is an odd number,

$$\frac{n!}{e} > a_n \stackrel{|d_n| < 1}{\Rightarrow} a_n = \left\lfloor \frac{n!}{e} \right\rfloor \quad (52)$$

If  $n$  is an even number,

$$\frac{n!}{e} < a_n \stackrel{|d_n| < 1}{\Rightarrow} a_n = \left\lceil \frac{n!}{e} \right\rceil \quad (53)$$

Therefore, the analytic expression of the total dislocation permutation number can be written as

$$a_n = \begin{cases} \left\lfloor \frac{n!}{e} \right\rfloor, n = 2k - 1, k \in N^* \\ \left\lceil \frac{n!}{e} \right\rceil, n = 2k, k \in N^* \end{cases} \quad (54)$$

### 3.2. Rationality verification

The total number of ways for  $n$  different ions to freely select  $n$  ion channels is  $n^n$ . Therefore, the probability of fully misaligned arrangement can be approximately expressed as:

$$P_n = \frac{1}{e} \times \frac{n!}{n^n} \quad (55)$$

It is not difficult to find that this probability monotonically decreases with respect to the number of ion channels  $n$ , which indicates that a greater number of ion channels can result in lower possibility of ion blockage. Note that the constant term  $P_1 = \frac{1}{e}$  in the expression of this probability is independent of ion channels and can be regarded as the probability of resting potential preconditions, which is that cells are in a state of reverse potential transport of ions. On the basis of Equation (55), the average probability of a single ion channel being blocked by a concentration gradient can be represented as:

$$\bar{p}_n = \frac{\sqrt[n]{n!}}{n} \quad (56)$$

From the biological point of view, the purpose of opening more ion channels is to achieve higher ion transport efficiency. In other words, the average probability of a single channel being blocked at a certain moment should be lower with more activated ion channels. Therefore, the rationality of the above probability model can be verified by the monotonicity proof of  $\bar{p}_n$ .

It should be noted that the sufficient condition for the monotonic increase of sequence  $\bar{p}_n$  can be expressed as:

$$\frac{\bar{p}_{n+1}}{\bar{p}_n} < 1 \Leftrightarrow (n+1) \times \sqrt[n]{n!} > n \times \sqrt[n+1]{(n+1)!} = n \times \sqrt[n+1]{(n+1) \times n!} \quad (57)$$

Taking the  $n(n+1)$  power on both sides of the above equation, it can be reducible to:

$$\frac{\bar{p}_{n+1}}{\bar{p}_n} < 1 \stackrel{a \in \mathbb{N}^+}{\Leftrightarrow} \left(1 + \frac{1}{n}\right)^n > \frac{n}{\sqrt[n]{n!}} \Leftrightarrow n \ln\left(1 + \frac{1}{n}\right) > -\frac{1}{n} \left[ \ln \frac{n}{n} + \ln \frac{n-1}{n} + \dots + \ln \frac{1}{n} \right] \quad (58)$$

It should be noticed that the expression on the right side of the above inequality has a special geometric meaning shown in **Figure 12** based on the definition of definite integral.

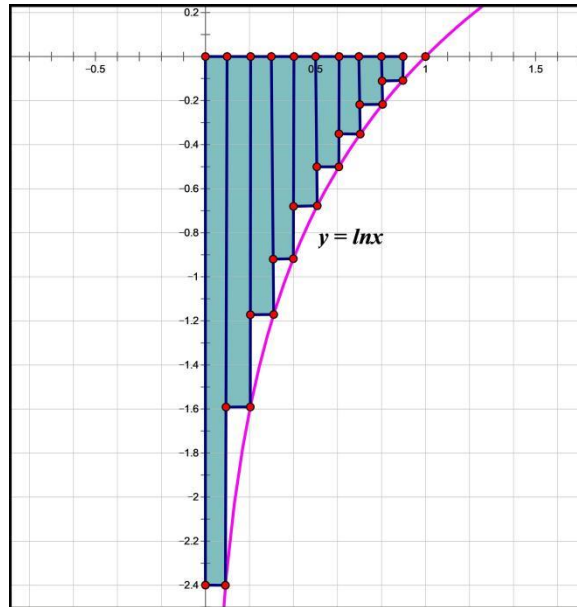


**Figure 12.** The integration process of logarithmic functions.

In specific, assuming that

$$S = -\frac{1}{n} \left[ \ln \frac{n}{n} + \ln \frac{n-1}{n} + \dots + \ln \frac{1}{n} \right] \quad (59)$$

its geometric meaning is areas sum of all blue rectangles. Therefore, it is easy to conclude that

$$-\int_0^1 \ln x \, dx > -\frac{1}{n} \left[ \ln \frac{n}{n} + \ln \frac{n-1}{n} + \dots + \ln \frac{1}{n} \right] = S \quad (60)$$

Besides,

$$-\int_0^1 \ln x \, dx = -\left( x \ln x - x \right) \Big|_0^1 = 1 + \lim_{x \rightarrow 0^+} x \ln x = 1 + \lim_{x \rightarrow 0^+} \frac{\ln x}{x^{-1}} = 1 + 0 = 1 \quad (61)$$

which indicates that the area enclosed by the graph and coordinate axis of function  $y = \ln x$  equals to 1. The power series expansion of  $\ln(1+x)$  can be expressed as:

$$\ln(1+x) = \frac{(-1)^0}{1} \times x + \frac{(-1)^1}{2} \times x^2 + \frac{(-1)^2}{3} \times x^3 + \dots, x \in (-1,1] \quad (62)$$

Therefore,

$$\ln\left(1 + \frac{1}{n}\right) = \frac{(-1)^0}{1} \times \frac{1}{n} + \frac{(-1)^1}{2} \times \frac{1}{n^2} + \frac{(-1)^2}{3} \times \frac{1}{n^3} + \dots, n \geq 1 \Rightarrow n \ln\left(1 + \frac{1}{n}\right) = \frac{(-1)^0}{1} \times 1 + \frac{(-1)^1}{2} \times \frac{1}{n} + \frac{(-1)^2}{3} \times \frac{1}{n^2} + \dots, n \geq 1 \quad (63)$$

It can be seen that the odd term in the above expression is greater than the next even term adjacent to it, which implies that

$$n \ln\left(1 + \frac{1}{n}\right) \rightrightarrows \frac{(-1)^0}{1} \times 1 + \frac{(-1)^1}{2} \times \frac{1}{n^1} = 1 - \frac{1}{2n} \quad (64)$$

Thus,

$$1 - \frac{1}{2n} > S \Leftrightarrow 1 - S > \frac{1}{2n} \quad (65)$$

is the sufficient condition for Equation (57). The geometric meaning of  $1 - S$  is the sum of blank areas in **Figure 12**, while  $\frac{1}{2n}$  represents the area of the yellow triangle in **Figure 13**. To be specific,

$$1 - S > S_{\Delta ABC} = \frac{1}{2} \times CA \times CB = \frac{1}{2} \times \frac{1}{n} \times h \quad (66)$$

where the gradient  $k$  of  $AB$  and the length  $h$  of line segment  $CB$  in **Figure 13** satisfying

$$\left. \begin{aligned} h &= \frac{1}{n} \times k, \\ k &= \left. \frac{d(\ln x)}{dx} \right|_{x=\frac{1}{n}} = \left. \frac{1}{x} \right|_{x=\frac{1}{n}} = n \end{aligned} \right\} \Rightarrow h = 1 \Rightarrow S_{\Delta ABC} = \frac{1}{2n} \quad (67)$$

Therefore,

$$n \ln\left(1 + \frac{1}{n}\right) > 1 - \frac{1}{2n} > S \Rightarrow \frac{\bar{p}_{n+1}}{\bar{p}_n} < 1 \quad (68)$$

This important theoretical result means that the average probability  $\bar{p}_n$  of a single channel being blocked at a certain moment decreases with the increasing number of activated ion channels  $n$ , which successfully proves the rationality of the probability model employed.

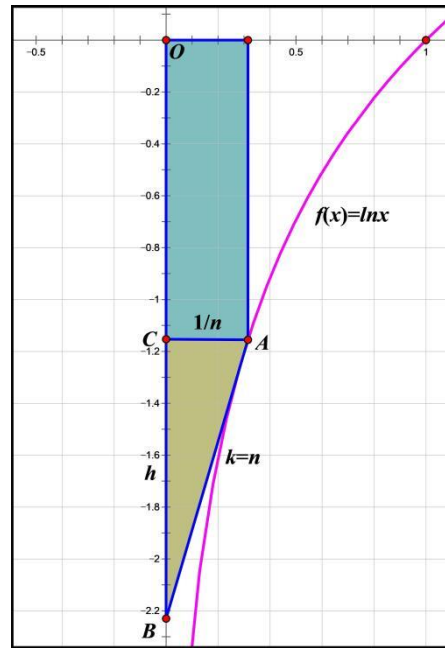


**Figure 13.** The unequal relationship of area micro-elements.

#### 4. Stress state analysis of myocardium

The preceding analysis has elucidated the mathematical mechanisms and biological significance of the resting potential within the cardiac cycle. However, for clinical advancements in cardiac research, it is also imperative to take account for the mechanical vibrations of the heart.

The elastic modulus and Poisson's ratio of the myocardium are critical indicators of heart health. Existing studies have suggested methods for experimentally measuring the elastic modulus using precision medical equipment such as MRI, yet have seldom discussed theoretical calculations. Furthermore, the experimental methods are economically costly, precluding their widespread application. Therefore, it is of great clinical value to provide a theoretical method to calculate the elastic modulus, Poisson's ratio, shear modulus and other material parameters of myocardium through low-cost measurement such as echocardiography. Based on this idea, several key issues to be solved in this chapter are as follows:

- 1) Establish an approximate mechanical model of ventricular muscle at the end of diastole and contraction;
- 2) Modify Laplace's law for stress calculation of thick wall objects;
- 3) Solve the three-dimensional stress state of the object under uniform pressure;
- 4) Derive the theoretical expression of myocardial material parameters.

##### 4.1. Mechanical model of ventricular muscle

The schematic diagram of blood flow of heart pump is shown in **Figure 14**. During the contraction of the left and right ventricles, oxygen-rich arterial blood and oxygen-poor venous blood are respectively pumped into aorta and pulmonary artery for systemic and pulmonary circulation. In this process, the mitral and tricuspid valves close, while the aortic and pulmonary valves open. Oxygen-poor venous blood from the systemic circulation flows into the right atrium through both the superior and

inferior vena cava, while the oxygen-rich arterial blood from the pulmonary circulation flows into the left atrium through the pulmonary vein. During the ventricular diastole, the aortic and pulmonary valves close, and the mitral and tricuspid valves open to facilitate the flow of blood from the atria into the ventricles.

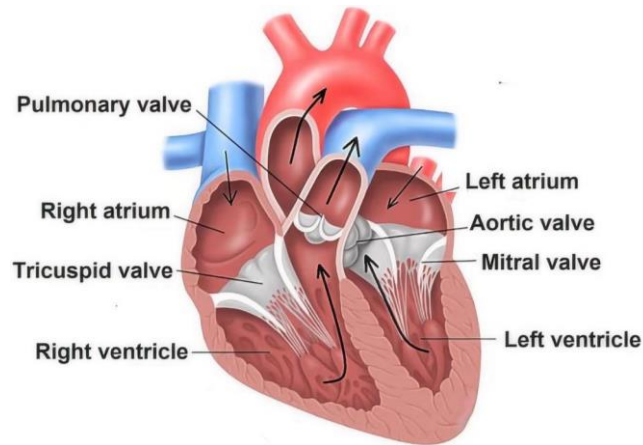


**Figure 14.** The schematic diagram of blood flow of heart pump.

Due to the high mortality rate associated with acute heart diseases like ventricular fibrillation, the mechanical properties of ventricular myocardium must be a primary focus of research. The end diastolic and end systolic phases of ventricular muscle correspond to the two extreme points of linear strain, which should be discussed respectively.

At the end of the diastolic phase, the ventricle's inner diameter enlarges, resembling a balloon being inflated. Therefore, the mechanical model can be described approximately using a spherical shell subjected to uniform pressure difference, as illustrated in **Figure 15**.

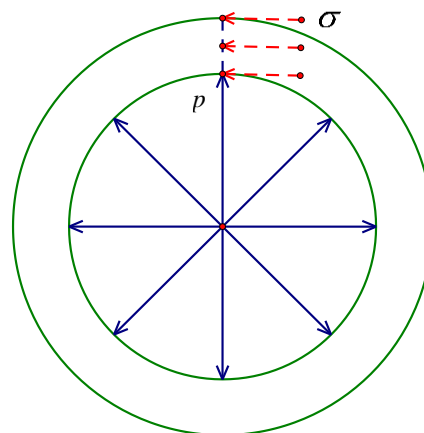


**Figure 15.** Spherical shell model under uniform pressure difference.

#### 4.2. Proof of Laplace's law

Laplace's law is frequently employed to compute the normal stress in spherical shell models. For the sake of theoretical completeness, its brief proof is presented as follows.

Due to symmetry, the resultant force produced by the uniform pressure difference must be along the y-axis direction. Take the annular micro area  $dA$  marked in red as shown in the **Figure 16**, and its value can be expressed as:

$$dA = dS \times 2\pi R \cos \theta. \quad (69)$$

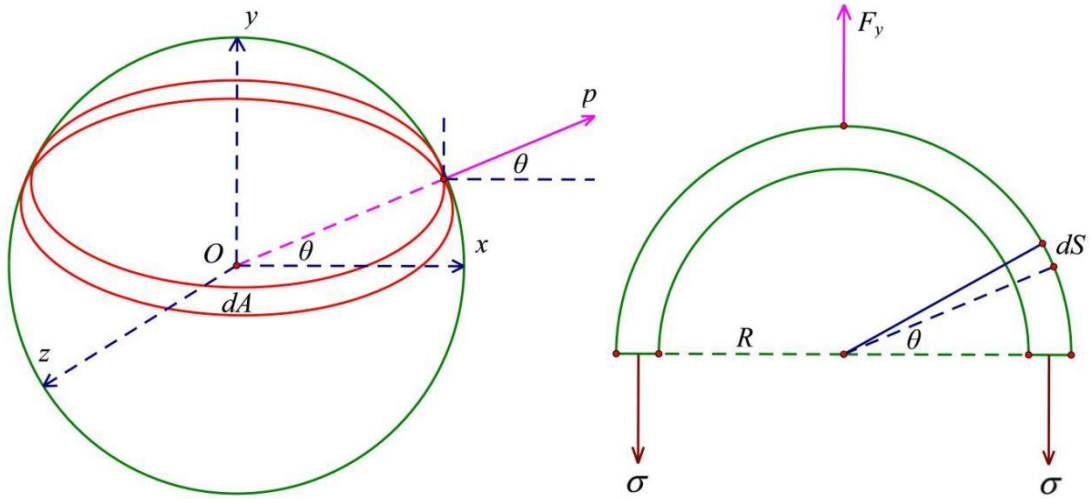


**Figure 16.** Laplace's law of thin-walled objects under uniform pressure.

The resultant force  $dF_y$  on the area element can be expressed as:

$$\begin{aligned} dF_y &= p(dA) \times \sin \theta \\ &= p(dS) \times 2\pi R \times \cos \theta \times \sin \theta \\ &= p(dS \times \cos \theta) \times (2\pi R \times \sin \theta) \\ &= p \times dy \times 2\pi y \\ &= (2\pi p y) dy. \end{aligned} \quad (70)$$

Therefore, the resultant force acting on the hemisphere can be expressed as:

$$F_y = \int_0^r 2\pi p y dy = \pi p r^2 \quad (71)$$

Ignoring the influence of thickness  $t$  on the normal stress distribution, the equilibrium equation in the y-axis direction of the hemisphere can be expressed as:

$$\pi p r^2 = \sigma \times (2\pi r t) \quad (72)$$

By simplifying the above Equation, the equivalent relationship between normal stress  $\sigma$  and pressure difference  $p$  can be obtained as:

$$\sigma = \frac{pr}{2t} \Leftrightarrow p = \frac{2\sigma t}{r} \quad (73)$$

which is named for Laplace's law.

### 4.3. Modified Laplace's law

According to the proof process of Laplace's law, its application scope is limited to thin-wall shells. However, the size of the ventricular wall cannot be ignored during the relaxation and contraction process of ventricular muscle. Therefore, in order to

study the stress distribution in ventricular wall, the Laplace's law has to be modified by considering the change of thickness.

The specific method is to employ the generalized Hooke's law to analyze the stress state of the unit cell on the external surface of the ventricular wall shown in **Figure 17**. Actually, the unit cell on inner surface exhibits the maximum normal stress due to its largest linear strain considering the decrease in ventricular wall thickness during diastole, which is consistent with the stress concentration theory. In brief, the inner surface of the ventricular wall is a dangerous location during diastole. However, the unit cell on the external surface instead of inner surface is selected as the analysis target to simplify the derivation of mathematical expressions.

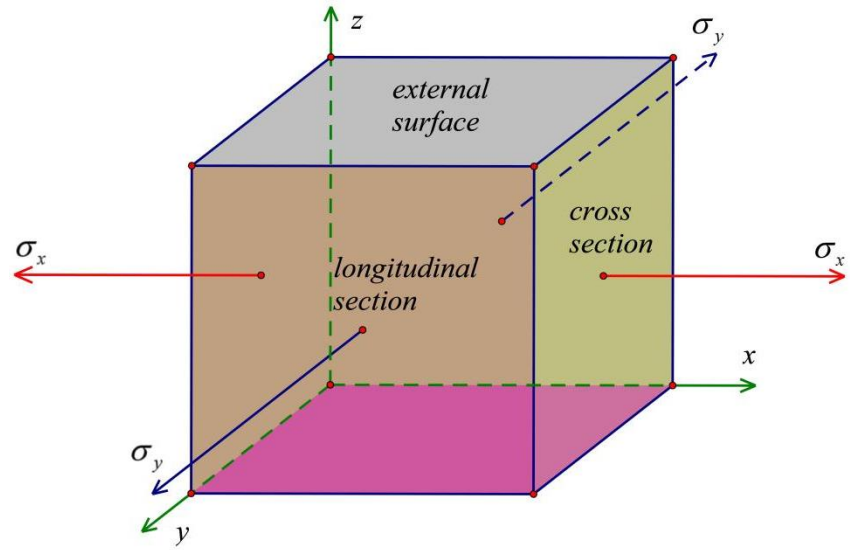


**Figure 17.** The unit cell on the inner surface of the ventricular wall.

As shown in **Figure 17**, there is no shear stress on the external surface. According to the reciprocal theorem of shear stress, there is no shear stress on each section of the unit cell. In fact, based on the centrosymmetry and axisymmetry of the sphere, any unit at any location on the spherical shell under uniform pressure experiences no shear stress. Symmetry also indicates that the normal stresses in both the cross and longitudinal sections are equal.

The initial radius and wall thickness of the ventricle in its natural state (no contractility) can be denoted as  $r_0$  and  $t_0$ , respectively. At a certain moment during diastole, the radius  $r$  of the ventricle should satisfy:

$$r > r_0 \quad (74)$$

which implies that ventricular muscles produce contractile force. The linear strain of a unit cell can be expressed by definition as:

$$\varepsilon_x = \varepsilon_y = \frac{2\pi r - 2\pi r_0}{2\pi r_0} = \frac{r}{r_0} - 1 > 0 \quad (75)$$

The expression of the generalized Hooke's law can be written as:

$$\begin{cases} \varepsilon_x = \frac{1}{E} [\sigma_x - \mu(\sigma_y + \sigma_z)] \\ \varepsilon_y = \frac{1}{E} [\sigma_y - \mu(\sigma_x + \sigma_z)] \\ \varepsilon_z = \frac{1}{E} [\sigma_z - \mu(\sigma_x + \sigma_y)] \end{cases} \quad (76)$$

in which  $E$  denotes elastic modulus while  $\mu$  represents Poisson's ratio of ventricular muscle. By substituting the conditions:

$$\begin{cases} \sigma_x = \sigma_y, \\ \sigma_z = 0 \end{cases} \quad (77)$$

it can be obtained that:

$$\begin{cases} \sigma_x = \sigma_y = \sigma = \frac{E(\frac{r}{r_0} - 1)}{1 - \mu} \\ \varepsilon_z = -\frac{2\mu\sigma}{E} = \frac{2\mu(1 - \frac{r}{r_0})}{1 - \mu} \end{cases} \quad (78)$$

Therefore, the Laplace's law can be modified as:

$$\begin{aligned} p &= \frac{2(1 + \varepsilon_z)t\sigma}{r} \\ &= \left\{ \frac{1}{r} \left[ 2t + \frac{4t\mu(1 - \frac{r}{r_0})}{1 - \mu} \right] \right\} \times \left[ \frac{E(\frac{r}{r_0} - 1)}{1 - \mu} \right] \\ &= \left\{ \frac{1}{r} \left[ 2t + \frac{4t\mu}{1 - \mu} \right] - \frac{4t\mu}{(1 - \mu)r_0} \right\} \times \left[ \frac{E}{(1 - \mu)r_0} \times r - \frac{E}{(1 - \mu)} \right]. \end{aligned} \quad (79)$$

It should be pointed out that if the thickness variation  $\varepsilon_z t$  of ventricular wall is not considered, the recovery pressure  $p$  of ventricular muscle will monotonically increase with respect to radius  $r$ , which is obviously inconsistent with the experimental conclusion.

#### 4.4. Calculation of Poisson's ratio based on the state of ventricular muscle at the end of diastole

At the end of diastole, the recovery pressure of the ventricular muscle reaches its peak, corresponding to the extremum point of the modified Laplace's law. Therefore, it is necessary to study its monotonicity. Through following substitution steps:

$$\left\{ \begin{array}{l} K_1 = 2t + \frac{4t\mu}{1-\mu} \\ K_2 = \frac{4t\mu}{(1-\mu)r_0} \\ K_3 = \frac{E}{(1-\mu)r_0} \\ K_4 = \frac{E}{(1-\mu)} \end{array} \right. \quad (80)$$

the modified Laplace's law can be simplified as follows:

$$p = \left(\frac{K_1}{r} - K_2\right) \times (K_3r - K_4) = K_1K_3 + K_2K_4 - \left(\frac{K_1K_4}{r} + K_2K_3r\right) \quad (81)$$

where  $K_i > 0, i = 1,2,3,4$ . From the mean inequality, it can be obtained that

$$p = K_1K_3 + K_2K_4 - \left(\frac{K_1K_4}{r} + K_2K_3r\right) \leq K_1K_3 + K_2K_4 - 2\sqrt{K_1K_2K_3K_4} \quad (82)$$

Therefore, the maximum point corresponding to the end diastolic dimension of the ventricular muscle should satisfy the following conditions:

$$\frac{K_1K_4}{r} = K_2K_3r \Rightarrow r = \sqrt{\frac{K_1K_4}{K_2K_3}} = \sqrt{\frac{(2t + \frac{4t\mu}{1-\mu}) \times \frac{E}{1-\mu}}{\frac{4t\mu}{1-\mu} \times \frac{1}{r_0} \times \frac{E}{1-\mu} \times \frac{1}{r_0}}} = r_0 \sqrt{1 + \frac{1-\mu}{2\mu}} \quad (83)$$

This finding indicates that, once the Poisson's ratio  $\mu$  of the ventricular muscle is known, the original size  $r_0$  of the ventricle in its natural state can be calculated.

According to the inference of generalized Hooke's law, the following conditions should be met between the volume strain  $\gamma$  and the principal stress of the unit cell:

$$\begin{aligned} \gamma &= \frac{\Delta V}{V} = \frac{4\pi r^2t - 4\pi r_0^2t_0}{4\pi r_0^2t_0} = \frac{r^2t}{r_0^2t_0} - 1 \\ &\approx \varepsilon_1 + \varepsilon_2 + \varepsilon_3 \\ &= \frac{(1-2\mu)}{E} (\sigma_1 + \sigma_2 + \sigma_3) \\ &= \frac{2\sigma(1-2\mu)}{E} \\ &= \frac{2(1-2\mu)(\frac{r}{r_0} - 1)}{1-\mu}. \end{aligned} \quad (84)$$

Therefore,

$$\frac{r^2t}{r_0^2t_0} - 1 \approx \frac{2(1-2\mu)(\frac{r}{r_0} - 1)}{1-\mu}, r > r_0 \quad (85)$$

Substituting the transform process:

$$\begin{cases} r^2 t = x, r = y, \\ A = \frac{1}{r_0^2 t_0}, B = \frac{2(2\mu - 1)}{(1 - \mu)r_0}, C = \frac{2(1 - 2\mu)}{(1 - \mu)} - 1 \end{cases} \quad (86)$$

Equation (85) can be simplified as:

$$Ax + By + C = 0 \quad (87)$$

which is obviously a plane equation in a spatial coordinate system. As indicated by the formula above, merely three sets of measurements for the ventricular radius and wall thickness during diastolic period ( $r > r_0$ ) are required to determine the initial size of the ventricle. It is important to note that the necessary dimensional data can be acquired solely through echocardiography, eliminating the need for MRI.

#### 4.5. The three-dimensional uniform pressure state of ventricular muscles during the end of systole

During systole, the external pressure on the ventricle exceeds its internal pressure, rendering modified Laplace's law inapplicable. Based on the superposition principle of small deformations, the pressure differential between the interior and exterior is bound to lead to further contraction of the ventricle. Therefore, at the end of systole, the ventricular wall is approximately in a state of uniform internal and external pressure (no contractile restitution force). To solve the stress state of the ventricular muscle at this time, it is necessary to prove the following lemma: Any point within the object subjected to uniform pressure is in a state of three-dimensional uniform stress, which is named as theory of three directional uniform stress state. Its proof process is as follows.

Firstly, the planar situation as shown in **Figure 18** should be considered. To be specific, for any point  $A$  within the circle, two non-perpendicular symmetrical sections marked in purple can be taken (with the line connecting the point to the circle's center as the axis of symmetry). From the symmetry, it is evident that the stress state on these two sections near the point can be represented in coordinates as  $(\sigma, \tau)$  and  $(\sigma, -\tau)$ . From the balance equation of the rectangle represented by the black dotted line, it can be concluded that there must be a principal plane at point  $A$  where the normal stress is  $-p$ .

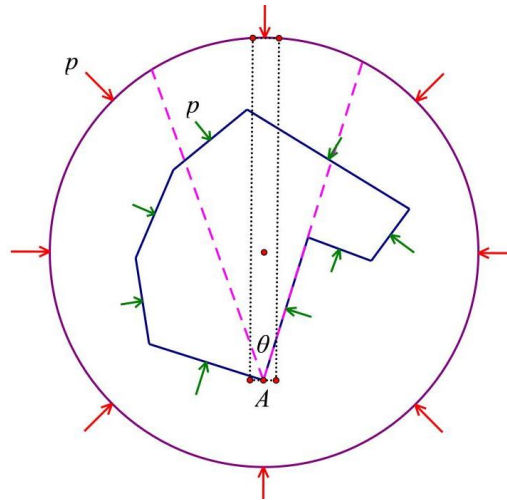


**Figure 18.** Schematic diagram of the two-dimensional pressure equalization theory.

If the shear stress  $\tau = 0$ , the pair of purple symmetrical section must be the principal planes near point  $A$ . According to the theory of stress circles, if the principal plane is not perpendicular, the unit cell must be in a state of uniform pressure (tension) in two directions, indicating that the radius of the stress circle is zero. If the shear stress  $\tau \neq 0$ , the two cross-sections represented by  $(\sigma, \tau)$  and  $(\sigma, -\tau)$  must be perpendicular, which contradicts the assumption. In summary, any point within a circle subjected to uniform pressure is in a state of two-way uniform pressure, which means that the stress circle with a radius of zero degenerates into a point, and all cross-sections in all directions are the principal planes:

$$\sqrt{\left(\frac{\sigma_x - \sigma_y}{2}\right)^2 + \tau_{xy}^2} = 0 \Rightarrow \sigma_x = \sigma_y, \tau_{xy} = 0 \quad (88)$$

For any shape of planar object subjected to uniform pressure, a circle subjected to uniform pressure can be employed as its envelope as shown in **Figure 18**. Any point inside the planar object must be located inside the pressure (tension) equalization envelope circle, therefore it must be in a pressure (tension) equalizing state as well.

By means of similar approach, the theory of three-dimensional pressure equalization on space objects can also be proved. Specifically, any point  $A$  within a uniform pressure sphere can be represented as the intersection of two perpendicular intersecting chords marked in purple as shown in **Figure 19**. By combining the central symmetry and axial symmetry of the sphere, it can be proven that there is no shear stress in any unit cell at any position inside the uniformly pressurized sphere. The equilibrium equation of the prism represented by the yellow dashed line indicates that the normal stress at point  $A$  on the cross-section is  $-p$ . Each purple chord and the spherical center can form a plane about which two non-perpendicular symmetric sections (plane  $\alpha$  and  $\beta$ ) passing through the chord can be introduced. Base on the proof process of the plane case shown in **Figure 18**, all points on the chord are in a two-way uniform pressure state on its normal plane. Similarly, it can be demonstrated that another chord perpendicular to this one also possesses this property. Therefore, the intersection point  $A$  of the two chords must be in the state of three-way uniform pressure.

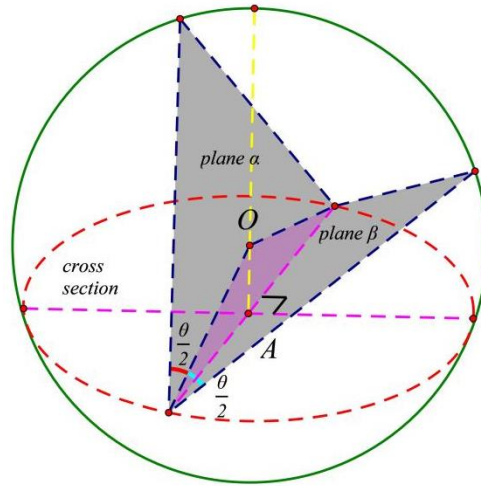


**Figure 19.** Schematic diagram of the three-dimensional pressure equalization theory.

The stress on any given cross-section of a spatial unit cell can be represented as:

$$\begin{cases} (\sigma_n - \frac{\sigma_2 + \sigma_3}{2})^2 + \tau_n^2 = (\frac{\sigma_2 - \sigma_3}{2})^2 + l^2(\sigma_1 - \sigma_2)(\sigma_1 - \sigma_3) \\ (\sigma_n - \frac{\sigma_3 + \sigma_1}{2})^2 + \tau_n^2 = (\frac{\sigma_3 - \sigma_1}{2})^2 - m^2(\sigma_2 - \sigma_3)(\sigma_1 - \sigma_2) \\ (\sigma_n - \frac{\sigma_1 + \sigma_2}{2})^2 + \tau_n^2 = (\frac{\sigma_1 - \sigma_2}{2})^2 + n^2(\sigma_1 - \sigma_3)(\sigma_2 - \sigma_3) \end{cases} \quad (89)$$

In above formulas,  $\sigma_n$  denotes the normal stress,  $\tau_n$  represents the shear stress, while  $l, m, n$  describe the cosine values of the angles formed by the normal to the cross-section and the three axes of the rectangular coordinate system, which satisfying:

$$l^2 + m^2 + n^2 = 1. \quad (90)$$

Specifically, for the case of three-way uniform pressure (tension), the following conditions should be met:

$$\begin{cases} (\sigma_n - \frac{\sigma_2 + \sigma_3}{2})^2 + \tau_n^2 = (\frac{\sigma_2 - \sigma_3}{2})^2 + l^2(\sigma_1 - \sigma_2)(\sigma_1 - \sigma_3) \\ (\sigma_n - \frac{\sigma_3 + \sigma_1}{2})^2 + \tau_n^2 = (\frac{\sigma_3 - \sigma_1}{2})^2 - m^2(\sigma_2 - \sigma_3)(\sigma_1 - \sigma_2) \\ (\sigma_n - \frac{\sigma_1 + \sigma_2}{2})^2 + \tau_n^2 = (\frac{\sigma_1 - \sigma_2}{2})^2 + n^2(\sigma_1 - \sigma_3)(\sigma_2 - \sigma_3) \\ \sigma_1 = \sigma_2 = \sigma_3 = p \end{cases} \Rightarrow \sigma_n = p, \tau_n = 0 \quad (91)$$

Based on three-way uniform pressure state at the end of ventricular systole, it can be concluded that at this moment, the normal stress in the ventricular muscle is approximately equal to the aortic blood pressure. It should be noted that currently, aortic blood pressure cannot be precisely measured through non-invasive methods, but it can be roughly estimated by brachial artery blood pressure.

## 5. Results

### 5.1. Calculation method and reference value of human ventricular elastic modulus

Based on all existing conclusions, the theoretical calculation formula for the elastic modulus of ventricular muscle can be already derived.  $P_d$  and  $P_s$  are used to represent diastolic and systolic blood pressure of aorta. Besides, employing  $\varepsilon_x^+$  and  $\varepsilon_z^-$  to denote the end diastolic circumferential strain and end systolic radial strain of the ventricle respectively, it can be concluded combing the generalized Hooke's law and pressure equalization theory that:

$$\begin{aligned}
 \varepsilon_z^- &= \frac{1}{E}[\sigma_z - \mu(\sigma_x + \sigma_y)] \\
 &= \frac{1}{E}[-P_s - \mu(-2P_s)] \\
 &= \frac{2\pi t_- - 2\pi t_0}{2\pi t_0} \\
 &= \frac{t_-}{t_0} - 1 \\
 \Rightarrow E &= \frac{(1-2\mu)P_s}{1 - \frac{t_-}{t_0}},
 \end{aligned} \tag{92}$$

and

$$\begin{aligned}
 \varepsilon_x^+ &= \frac{1}{E}[\sigma_x - \mu(\sigma_y + \sigma_z)] \\
 &= \frac{1}{E}[P_d - \mu(P_d + 0)] \\
 &= \frac{2\pi r_+ - 2\pi r_0}{2\pi r_0} \\
 &= \frac{r_+}{r_0} - 1 \\
 \Rightarrow E &= \frac{(1-\mu)P_d}{\frac{r_+}{r_0} - 1} \\
 &= \frac{(1-\mu)P_d}{\sqrt{1 + \frac{1-\mu}{2\mu}} - 1} \\
 &= \frac{(1-\mu)P_d}{\sqrt{\frac{1}{2} + \frac{1}{2\mu}} - 1}.
 \end{aligned} \tag{93}$$

It should be noted that the numerator and denominator of Equation (92) are small, which has high requirements for measurement accuracy. Therefore, Equation (93) is more suitable for estimation. The aortic diastolic blood pressure  $P_d$  can be approximated by brachial artery blood diastolic pressure. Besides,  $r_+$  can be obtained through echocardiography while  $r_0$  and  $\mu$  can be calculated by Equation (85).

In fact, the systolic strain is influenced by various factors, including but not limited to blood pressure, myocardial function, mechanical bio-electric coupling behaviors, feedback mechanisms, abnormal structures under pathological conditions and so on. Besides, the pumping function of the heart involves the coordinated operation of multiple systems and can be influenced by various external factors, such as the differences in metabolic rate, hormone levels, and environmental force fields caused respectively by age, gender, and left ventricle load conditions. If all these individualized factors with significant differences are taken into account, the theoretical model will become exceptionally complex.

In order to balance the accuracy and simplicity of the theoretical model, we choose the main factors to consider, which is the stress and deformation of the myocardium in its natural state at the end of diastole. Therefore, we abandon the end systolic based approach mainly due to the involvement of autonomous cardiac contraction function, while the natural myocardial function in the calculation model based on the end diastolic can be described by Poisson's ratio.

## 5.2. Reference value of human ventricular elastic modulus

In order to verify the validity of the above theoretical calculation formula for elastic modulus of human ventricular muscle, for all variables involved, their median and boundary values of reference ranges based on echocardiography sampling data are employed to calculate the theoretical value so as to compare it with the experimental data. However, due to the lack of noninvasive detection methods for human hearts, the existing studies can only provide experimental measurement data of the elastic modulus of isolated pig hearts. The three-dimensional multivariate function image of ventricular muscle elastic modulus based on sampled data is shown in the **Figure 20**.

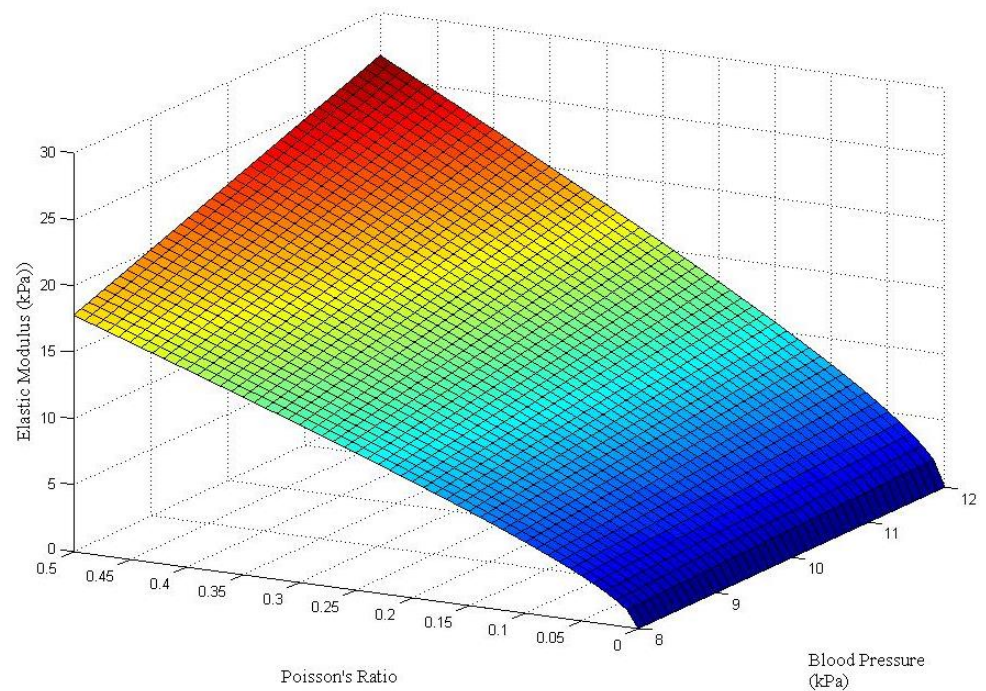


**Figure 20.** The 3-D multivariate function image of ventricular muscle elastic modulus based on echocardiography sampling data.

It should be noted that the interval of the sampled data shown in **Figure 20** already includes simple pathological conditions, such as abnormal Poisson’s ratio and blood pressure. However, the reliability of these data is based on the absence of organic lesions and structural damage to the heart. Therefore, strictly speaking, this calculation method based on echocardiography data cannot replace personalized diagnosis and treatment methods such as MRI. However, due to its relatively low price and relatively simple examination procedure, it may become a routine physical examination screening item for cardiovascular diseases. Some boundary and median data with reference value in **Figure 20** are listed in **Table 1**.

**Table 1.** Characteristic boundary and median values from echocardiography sampling data.

Poisson’s ratio (dimensionless)	Brachial artery blood pressure (mmHg)	Elastic modulus (kPa)
0.2	60	8.7420
0.2	75	10.9275
0.2	90	13.1130
0.45	60	16.3387
0.45	75	20.4234
0.45	90	24.5081
0.5	60	17.7979
0.5	75	22.2474
0.5	90	26.6969

By sampling a large number of echocardiography cases, the Poisson’s ratio range of human ventricular muscle can be estimated to be approximately [0.45,0.5]. Additionally, the reference range for human brachial artery diastolic pressure is [60,90] mmHg (or [8,12] kPa). The monotonicity of the elastic modulus function with respect to Poisson’s ratio can be determined by the following stagnation point conditions:

$$\frac{dE}{\mu} = \frac{(1 - \sqrt{\frac{1}{2}(1 + \frac{1}{\mu})}) - \frac{1}{2} \times \frac{-\frac{1}{2} \times \frac{1}{\mu^2}}{\sqrt{\frac{1}{2}(1 + \frac{1}{\mu})}} (1 - \mu)}{[\sqrt{\frac{1}{2}(1 + \frac{1}{\mu})} - 1]^2} \sqrt{\frac{1}{2}(1 + \frac{1}{\mu})} = U \quad 0 \Rightarrow U = 1 \Rightarrow \mu = 1 \quad (94)$$

Therefore, in the reference range, the elastic modulus function monotonically decreases with respect to Poisson’s ratio. By means of substituting the boundary values of all involved variables into Equation (93), the reference range of the radial elastic modulus of human ventricular muscle can be obtained as [16.3387,26.6969]kPa, which is consistent with the experimental data 20 kPa of isolated pig heart reported in literature [15–17], etc.

## 6. Discussion

### 6.1. The causes of differences in experimental data

There are great differences in the experimental data of the elastic modulus of isolated pig hearts in different references. The reasons are various, including sample selection, loading methods, etc. However, we believe that the main reason is the overload caused by the lack of clear external load limit in the tensile test. In other words, overload will cause irreversible damage to the physiological structure of the myocardium, so that the measured value of the elastic modulus is not the actual value of the myocardium in the working state. To be specific, the branched structure of cardiac muscle is shown in **Figure 21**.

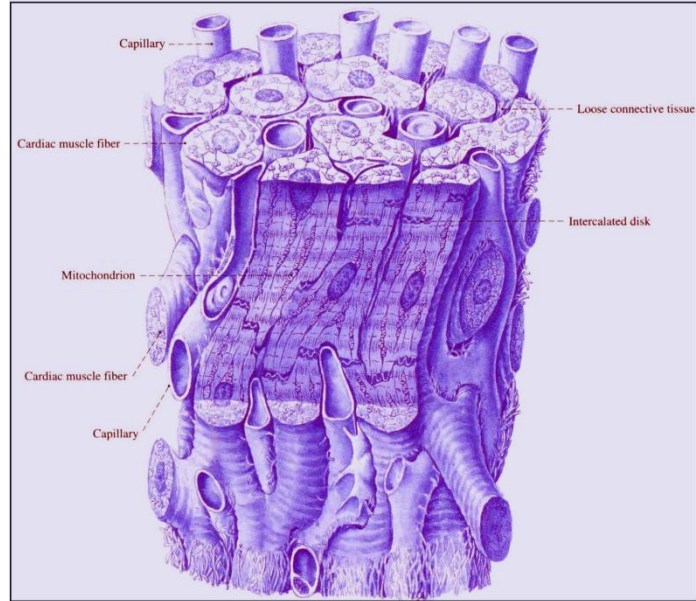


**Figure 21.** The branched structure of cardiac muscle.

The two ends of myocardia are linked by intercalated disk. There are capillaries and loose connective tissues between myocardia. The loose connective tissues mainly consist of collagen fibers and elastic fibers. The collagen can constitute the myocardial collagen network. The elastic fibers can cross myocardia in various directions. Therefore, if excessive external load destroys other myocardial structures in vitro, the measured elastic modulus data is likely to correspond to the straightened fibers instead of actual value of myocardial working state. This conclusion is consistent with the experimental results in reference [17].

## 6.2. Anisotropy of myocardium

A single myocardial fiber itself should be a kind of isotropic material, but due to the structural characteristics, bundles of myocardial fibers as a whole can exhibit anisotropic material properties. Longitudinal strain is more reproducible indeed due to its higher sensitivity to damage. Therefore, we are ought to consider and estimate the difference between the longitudinal elastic modulus and the radial elastic modulus. The theoretical method we use is to approximate the longitudinal elastic modulus using the radial shear modulus:

$$E_{radial} \approx G = \frac{E_{longitudinal}}{2(1 + \mu)} \quad (95)$$

The specific calculation process of error is as follows:

$$\begin{aligned}
 \frac{\varepsilon_{theoretical}}{\varepsilon_{practical}} &\approx \frac{\frac{1}{E} \times \sigma - \frac{\mu}{E} \times \sigma + \frac{\mu}{E} \times \frac{\sigma}{2} \times \frac{2t}{D}}{G \times \frac{\sigma}{2} - \frac{\mu}{E} \times \sigma + \frac{\mu}{E} \times \frac{\sigma}{2} \times \frac{2t}{D}} \\
 &= \frac{G = \frac{2(1+\mu)}{E} \left( 1 - \mu + \frac{t}{D} \mu \right)}{1 - \frac{\mu}{2} + \frac{t}{D} \mu} \\
 &= \frac{t=D}{1 + \frac{\mu}{2}} \stackrel{\mu \approx 0.5}{\approx} 0.8,
 \end{aligned} \tag{96}$$

where  $t$  and  $D$  respectively represent the thickness and diameter of myocardial bundle. It can be seen that based on the generalized Hooke's law, the ratio of the calculation results under the assumptions of isotropy and anisotropy equals approximately to 0.8. However, this truncation error can be offset to some extent considering the blood pressure error between the aorta and the brachial artery applied in our in the calculation.

### 6.3. Idealized assumptions

In order to avoid overly complex theoretical deductions and reduce dependence on experimental data, the theoretical model in this paper has made some idealized assumptions:

- 1) The ventricle can be regarded as a uniform thin-walled spherical shell;
- 2) The end diastolic period corresponds exactly to the extreme point of the pressure inside the ventricle;
- 3) Brachial artery blood pressure is close to aortic blood pressure;
- 4) The stress state of the unit body at each position of the ventricular wall is similar or exhibits a linear distribution, which can be approximated by the average value;
- 5) Stress distribution satisfies superposition principle;
- 6) The longitudinal shear modulus of myocardial bundles can be approximated by the radial elastic modulus.

These assumptions indicates that there exist some limitations of this calculation about to be addressed. Firstly, the calculation method may be invalid for some hypertensive patients because the abnormality of brachial artery blood pressure may be caused by non-cardiogenic factors, such as vascular organic damage. Generally speaking, the ventricular muscle material parameters of patients with cardiogenic diseases will change synchronously. Thus, for these cases, it is necessary to consider the measured Poisson's ratio for further diagnosis.

Secondly, the calculation method can only reflect the overall health status of ventricular muscle, and cannot find local lesions. Therefore, it can only be applied as a primary screening method for the prevention of acute heart disease, and cannot replace the diagnostic methods such as magnetic resonance imaging.

## 7. Conclusions

A new probability model is proposed to describe the resting potential and calculate its duration. This model has proven its capacity to evaluate the rationality of bioelectricity model based on the analysis of non-smooth dynamics involved in this paper. Besides, the theoretical calculation method of elastic modulus of human ventricular muscle is established and the reference value is provided. This calculation method based on the data of cardiac ultrasound, enables the large-scale screening of myocardial elastic modulus in the form of routine physical examination, which can reflect the heart health conditions. Therefore, it has important clinical value for the primary diagnosis and effective prevention of cardiogenic diseases at least. The research methodologies along with the conclusion framework of this article can be visualized as a flowchart shown in **Figure 22**.

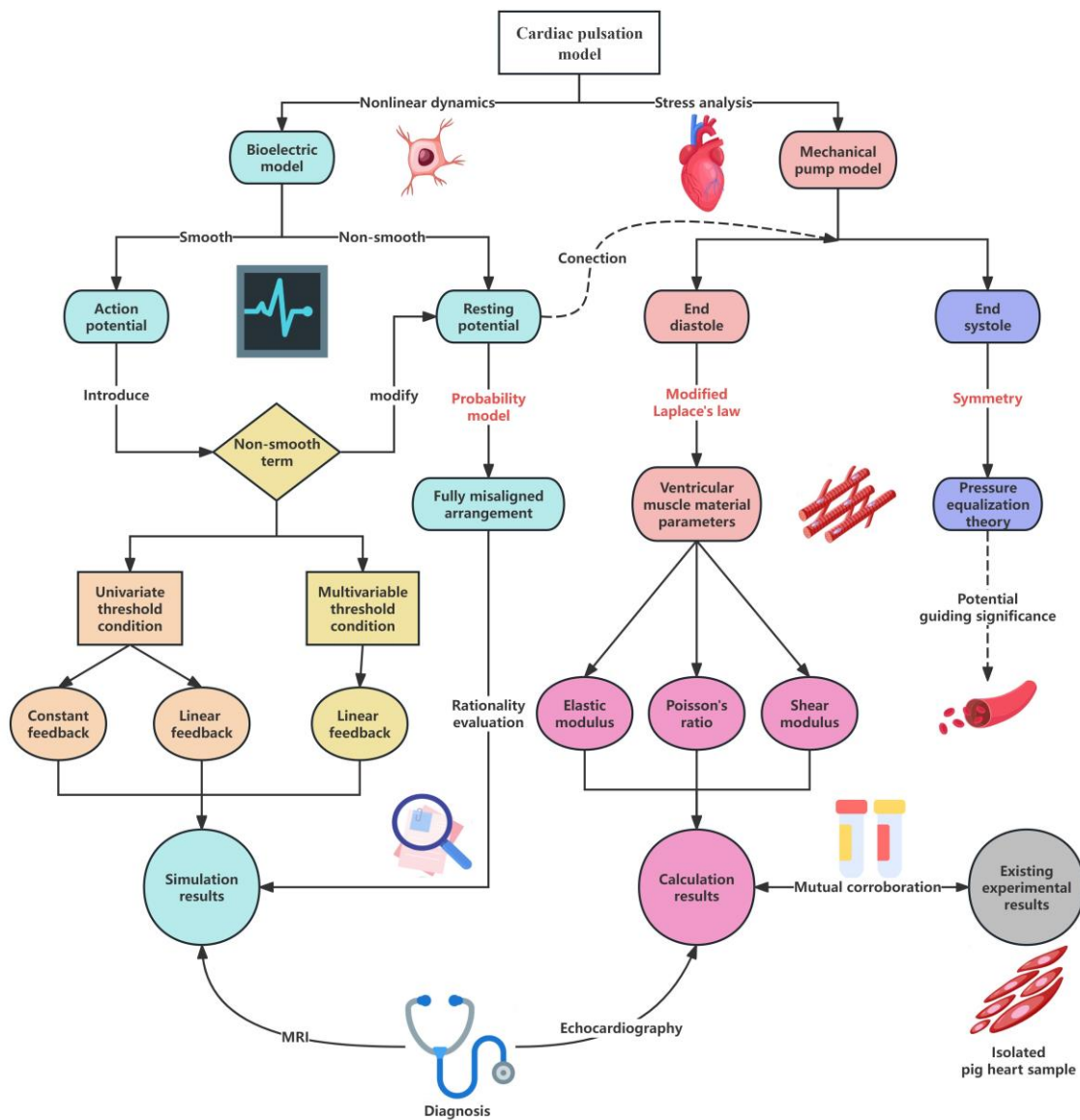


**Figure 22.** The framework of research methodologies and conclusions.

**Author contributions:** Conceptualization, RQ and XX; methodology, RQ; software, RQ; validation, RQ and XX; data curation, XX; writing—original draft preparation, RQ; writing—review and editing, RQ and XX; visualization, RQ; project administration, RQ; funding acquisition, RQ. All authors have read and agreed to the published version of the manuscript.

**Ethical approval:** Not applicable.

**Funding:** This research is supported by National Natural Science Foundation of China (Grant no. 12302012).

**Data availability:** All the data used to support the findings of this study are available from the corresponding author upon request.

**Conflict of interest:** The authors declare no conflict of interest.

## References

1. Smoluk L.T. and Protsenko Yu.L., Mechanical properties of passive myocardium: experiment and mathematical model, *Biophysics*, 2010, 55(5), pp. 796–799.
2. Hasan A., Ragaert K., Swieszkowski W., et al, Biomechanical properties of native and tissue engineered heart valve constructs, *J. Biomech.*, 2014, vol. 47, pp. 1949–1963.
3. Ostrovskiy N.V., Chelnokova N.O., Golyadkina A.A., et al, Biomechanical parameters of ventricles of the human heart, *Fund. Issled.*, 2015, nos. 1–10, pp. 2070–2075.
4. Chabiniok R. , Wang V.Y., Hadjicharalambous M., Asner L. , Lee J., Sermesant M. , et al, Multiphysics and multiscale modelling, data–model fusion and integration of organ physiology in the clinic: ventricular cardiac mechanics, *Interface Focus*, 2016, 6 (2), Article 20150083.
5. Shmurak M.I., Kuchumov A.G., and Voronova N.O., Hyperelastic models analysis for description of soft human tissues behavior, *Master’s J.*, 2017, no. 1, pp. 230–243.
6. Wang V.Y., Lam H., Ennis D.B., et al, Nash modelling passive diastolic mechanics with quantitative MRI of cardiac structure and function, *Med Image Anal*, 2009, 13(5), pp. 773–784.
7. Nordsletten D., Capilnasiu A., Zhang W., Wittgenstein A., Hadjicharalambous M., Sommer G., et al, A viscoelastic model for human myocardium, *Acta Biomater*, 2021, vol. 135, pp. 441–457.
8. Sommer G., Schriefl A.J., Andrä M., Sacherer M., Viertler C., Wolinski H., et al, Biomechanical properties and microstructure of human ventricular myocardium, *Acta Biomater*, 2015, vol. 24, pp. 172–192.
9. Rajagopal K., Hajian D.N., Natiq H., et al., Effect of Gaussian gradient in the medium's action potential morphology on spiral waves, *APPL MATH COMPUT*, 2024, vol. 470, Article 128590.
10. Hayashi T., Tokihiro T., Kurihara H., Yasuda K., Community effect of cardiomyocytes in beating rhythms is determined by stable cells, *Sci. Rep.*, 2017, vol. 7, Article 15450.
11. Tabi C.B., Dynamical analysis of the FitzHugh-Nagumo oscillations through a modified Van der Pol equation with fractional-order derivative term, *Int. J. Non-Linear Mech.*, 2018, vol. 105, pp. 173–178.
12. Yuan L., Liu Z.Q., Zhang H.M., et al, Noise-induced synchronous stochastic oscillations in small scale cultured heart-cell networks, *Chin. Phys. B*, 2011, 20 (2), Article 020508.
13. Qu R., Xia X., Wu G.Q., et al, Bursting Oscillation Mechanisms of a Desktop Medical Shaker with Eccentric Turntables Affected by Dry Friction. *Shock & Vibration*, 2023, vol. 2023, Article 8374444.
14. Qu R., Li S.L., Attractor and Vector Structure Analyses of Bursting oscillation with sliding bifurcation in filippov systems, *Shock & Vibration*, 2019, pp. 1–10.
15. Muslova S.A., Lotkovb A.I., Arutyunova S.D., and Albakova T.M., Calculation of the parameters of mechanical properties of the heart muscle, *Inorganic Materials: Applied Research*, 2021, 12(2), pp.433–44.
16. Latorre M., Montáns F.J., Wypiyw hyperelasticity without inversion formula: application to passive ventricular myocardium, *Comput Struct*, 2017, vol. 185, pp. 47–58.

17. Laita N., Rosales R.M., Wu M., et al, On modeling the in vivo ventricular passive mechanical behavior from in vitro experimental properties in porcine hearts, *Comput Struct*, 2024, vol. 292, Article 107241.
18. Ghanta R.K., Pugazenthi A., Zhao Y.G., et al, Influence of supraphysiologic biomaterial stiffness on ventricular mechanics and infarct reinforcement, *Acta BIOMATERIALIA*, 2022, vol. 149, pp. 30-39.
19. Liu W.Q., Nguyen-Truong M., LeBar K., et al, Multiscale contrasts between the right and left ventricle biomechanics in healthy adult sheep and translational implications, *Front BIOENG biotech*, 2022, vol. 105, Article 857638.
20. Park C.K., Kim J., Development of a three-dimensional- printed heart model replicating the elasticity, tear resistance, and hardness of pig heart using Agilus and Tango, *J MECH MED BIOL*, 2022, 22(3).
21. Peyronnet R., Desai A., Edelmann J.C., et al, Simultaneous assessment of radial and axial myocyte mechanics by combining atomic force microscopy and carbon fibre techniques, *PHILOS T R SOC B*, 2022, 377(1864).
22. Motchon Y.D., Sack K.L., Sirry M.S., et al, Effect of biomaterial stiffness on cardiac mechanics in a biventricular infarcted rat heart model with microstructural representation of in situ intramyocardial injectate, *INT J NUMER METH BIO*, 2023, 39(5).

## Appendix A. Supplementary description of pressure equalization theory

Although the pressure equalization theory cannot be directly used to calculate the material parameters of ventricular muscle, its conclusion has potential guiding significance for the stress analysis of blood vessels. Therefore, it is necessary to provide some supplements to this theory.

The spherical envelope method is employed in the proof part of pressure equalization theory. Actually, asymmetrical convex polyhedron can also be used to envelope the research object, which can be composed of several tetrahedrons as basic elements. In other words, a balanced tetrahedron subjected to uniform pressure  $\mathbf{p}$  on each side  $S_1, S_2, S_3$  has a determined resultant force  $\mathbf{F}_4$  on the bottom surface  $S_4$ , as shown in **Figure A1**. The resultant force  $\mathbf{F}_4 = \mathbf{p}' \times S_4$  is equivalent to the uniform load  $\mathbf{p}$  distributed on the bottom surface. According to the relevant theories of statics, the resultant force on the bottom shall meet the following conditions:

- 1) The principal vector equals to  $\mathbf{p} \times S_4$ ;
- 2) The principal moment is zero (Both bending moment and torque are zero);
- 3) The acting point is the geometric center of the bottom surface.

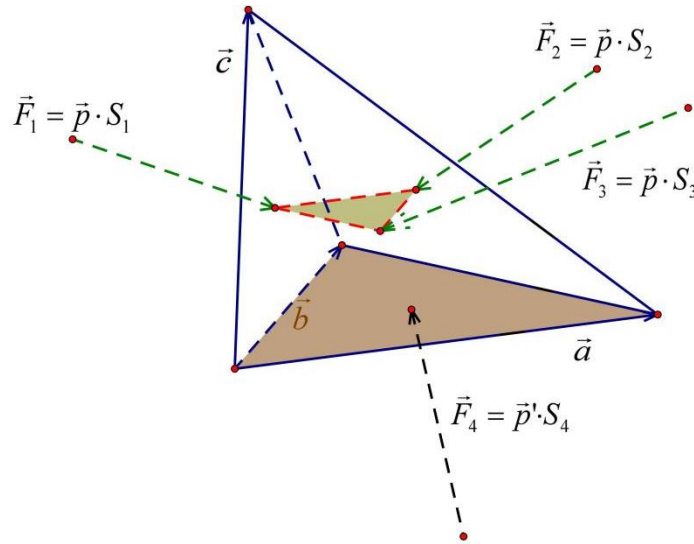


**Figure A1.** The tetrahedron under uniform pressure.

### I. Principal vector

Assuming  $p = 1$ , the external force on each side can be expressed as:

$$\begin{cases} \mathbf{F}_1 = \mathbf{b} \times \mathbf{c} \\ \mathbf{F}_2 = (\mathbf{b} - \mathbf{c}) \times (\mathbf{a} - \mathbf{b}) \\ \mathbf{F}_3 = \mathbf{c} \times \mathbf{a} \\ \mathbf{F}_4 = \mathbf{a} \times \mathbf{b} \end{cases} \quad (1)$$

Substituting above formulas to the equilibrium equation:

$$\mathbf{F}_1 + \mathbf{F}_2 + \mathbf{F}_3 + \mathbf{F}_4 = \mathbf{0} \quad (2)$$

it can be obtained that:

$$p' = 1 = p \quad (3)$$

The above conclusion can also be extended to the general pyramid shown in **Figure A2** as:

$$\left. \begin{aligned}
 \mathbf{F}_1 &= \mathbf{a}_1 \times \mathbf{b} \\
 \mathbf{F}_2 &= \mathbf{a}_2 \times (\mathbf{b} - \mathbf{a}_1) = \mathbf{a}_2 \times \mathbf{b} + \mathbf{a}_1 \times \mathbf{a}_2 \\
 \mathbf{F}_3 &= \mathbf{a}_3 \times (\mathbf{b} - \mathbf{a}_1 - \mathbf{a}_2) \\
 \mathbf{F}_4 &= \mathbf{a}_4 \times (\mathbf{b} - \mathbf{a}_1 - \mathbf{a}_2 - \mathbf{a}_3) \\
 &\dots \\
 \mathbf{F}_{n-1} &= \mathbf{a}_{n-1} \times (\mathbf{b} - \mathbf{a}_1 - \mathbf{a}_2 - \mathbf{a}_3 - \dots - \mathbf{a}_{n-2}) \\
 \mathbf{F}_n &= \mathbf{a}_n \times (\mathbf{b} - \mathbf{a}_1 - \mathbf{a}_2 - \mathbf{a}_3 - \dots - \mathbf{a}_{n-2} - \mathbf{a}_{n-1}) \\
 \mathbf{F}_{n+1} &= -\mathbf{a}_1 \times \mathbf{a}_2 - (\mathbf{a}_1 + \mathbf{a}_2) \times \mathbf{a}_3 - (\mathbf{a}_1 + \mathbf{a}_2 + \mathbf{a}_3) \times \mathbf{a}_4 - \dots - (\mathbf{a}_1 + \mathbf{a}_2 + \mathbf{a}_3 + \dots + \mathbf{a}_{n-2}) \times \mathbf{a}_{n-1}
 \end{aligned} \right\} \Rightarrow \sum_{i=1}^{n+1} \mathbf{F}_i = \mathbf{0} \quad (4)$$

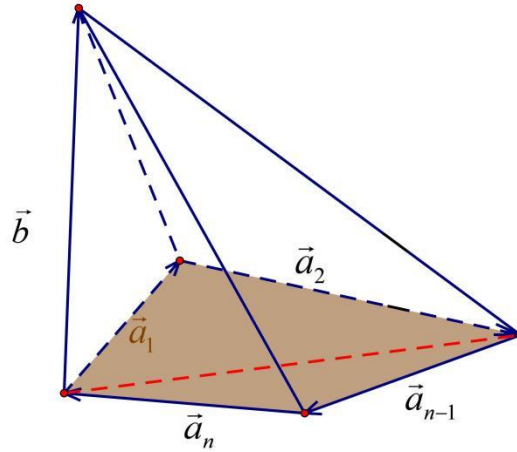


Figure A2. The general pyramid under uniform pressure.

## II. Torque

The normal component  $\mathbf{F}_{1\perp}, \mathbf{F}_{2\perp}, \mathbf{F}_{3\perp}$  and tangential component  $\mathbf{F}_{1//}, \mathbf{F}_{2//}, \mathbf{F}_{3//}$  can be obtained by projecting  $\mathbf{F}_1, \mathbf{F}_2, \mathbf{F}_3$  onto the plane of the yellow triangle formed by the centroids of all sides shown in Figure 21. From the equilibrium equations:

$$\begin{cases} \mathbf{F}_{1//} + \mathbf{F}_{2//} + \mathbf{F}_{3//} = \mathbf{0} \\ \mathbf{F}_{1\perp} + \mathbf{F}_{2\perp} + \mathbf{F}_{3\perp} = -\mathbf{F}_4 \end{cases} \quad (5)$$

it is clear that the tangential components have already formed a balance force system and the normal component can only generate bending moments. Therefore, the torque on the bottom surface has to be zero.

## III. Bending moments

Applying the translation theorem of force, the acting point of  $\mathbf{F}_1, \mathbf{F}_2, \mathbf{F}_3$  can be moved to bottom centroid. Since the torque is zero, the sum of the additional couple moments must be equal to the sum of the bending moments. The displacement vectors from the bottom centroid to each side centroid can be denoted as  $\mathbf{k}_1, \mathbf{k}_2, \mathbf{k}_3$ . From the geometric relationship in Figure 21, it is not difficult to deduct the expression of the displacement vectors as:

$$\begin{cases} \mathbf{k}_1 = \frac{1}{3}(\mathbf{b} + \mathbf{c}) - \frac{1}{3}(\mathbf{a} + \mathbf{b}) = \frac{1}{3}(\mathbf{c} - \mathbf{a}) \\ \mathbf{k}_2 = \frac{1}{3}\mathbf{c} \\ \mathbf{k}_3 = \frac{1}{3}(\mathbf{a} + \mathbf{c}) - \frac{1}{3}(\mathbf{a} + \mathbf{b}) = \frac{1}{3}(\mathbf{c} - \mathbf{b}) \end{cases} \quad (6)$$

Combining the expression of force vector (95), the sum of the additional couple moments can be expressed as:

$$\sum_{i=1}^3 \mathbf{k}_i \times \mathbf{F}_i = -\frac{1}{3} [\mathbf{a} \times (\mathbf{b} \times \mathbf{c}) + \mathbf{c} \times (\mathbf{a} \times \mathbf{b}) + \mathbf{b} \times (\mathbf{c} \times \mathbf{a})] \quad (7)$$

By establishing a spatial coordinate system and representing vectors in coordinates, it can be obtained that:

$$\begin{aligned} \mathbf{a} \times \mathbf{b} &= \begin{vmatrix} \mathbf{i} & \mathbf{j} & \mathbf{k} \\ x_a & y_a & z_a \\ x_b & y_b & z_b \end{vmatrix} = (y_a z_b - y_b z_a, x_b z_a - x_a z_b, x_a y_b - x_b y_a) \Rightarrow \mathbf{c} \times (\mathbf{a} \times \mathbf{b}) \\ &= \begin{vmatrix} \mathbf{i} & \mathbf{j} & \mathbf{k} \\ x_c & y_c & z_c \\ y_a z_b - y_b z_a & x_b z_a - x_a z_b & x_a y_b - x_b y_a \end{vmatrix} \\ &= (y_c x_a y_b - y_c x_b y_a - z_c x_b z_a + z_c x_a z_b, z_c y_a z_b - z_c y_b z_a - x_c x_a y_b + x_c x_b y_a, x_c x_b z_a - x_c x_a z_b \\ &\quad - y_c y_a z_b + y_c y_b z_a). \end{aligned} \quad (8)$$

According to the symmetry of rotation, it can be inferred that:

$$a \rightarrow c, b \rightarrow a, c \rightarrow b,$$

$$\begin{aligned} \mathbf{b} \times (\mathbf{c} \times \mathbf{a}) &= (y_b x_c y_a - y_b x_a y_c - z_b x_a z_c + z_b x_c z_a, z_b y_c z_a - z_b y_a z_c - x_b x_c y_a + x_b x_a y_c, \\ &\quad x_b x_a z_c - x_b x_c z_a - y_b y_c z_a + y_b y_a z_c). \end{aligned} \quad (9)$$

Similarly, it can be known that:

$$a \rightarrow b, b \rightarrow c, c \rightarrow a,$$

$$\begin{aligned} \mathbf{a} \times (\mathbf{b} \times \mathbf{c}) &= (y_a x_b y_c - y_a x_c y_b - z_a x_c z_b + z_a x_b z_c, z_a y_b z_c - z_a y_c z_b - x_a x_b y_c + x_a x_c y_b, \\ &\quad x_a x_c z_b - x_a x_b z_c - y_a y_b z_c + y_a y_c z_b). \end{aligned} \quad (10)$$

Summing up all above expressions (102), (103) and (104), it can be concluded that:

$$\sum_{i=1}^3 \mathbf{k}_i \times \mathbf{F}_i = -\frac{1}{3} [\mathbf{a} \times (\mathbf{b} \times \mathbf{c}) + \mathbf{c} \times (\mathbf{a} \times \mathbf{b}) + \mathbf{b} \times (\mathbf{c} \times \mathbf{a})] = \mathbf{0} \quad (11)$$

Therefore, there is no bending moment on the bottom surface.

It should be pointed that the above resultant force analysis does not mean that the stress on the bottom is uniformly distributed. In fact, the translation theorem of force can only be used to analyze the balance but not the deformation of deformed bodies. In other words, concentrated force and uniform load are equivalent only in the sense of equilibrium with the ignorance of deformation.

## Appendix B. The physical or physiological meanings of mathematical symbols

A large number of mathematical symbols are employed in the theoretical derivation process of this paper. The specific meaning of each mathematical symbol has been clearly explained in the text. For ease of reference, the physical or physiological meanings of frequently used mathematical symbols in bioelectric model and mechanical pump model are listed in **Tables B1** and **B2** respectively.

**Table B1.** Physical or physiological meaning of mathematical symbol used in bioelectric model.

Mathematical symbol	Physical/Physiological meaning
$x$	Membrane potential
$y$	Quick recovery current
$z$	Slow-varying adaptive current
$W$	External stimulation current
$A$	External excitation amplitude
$\Omega$	External excitation frequency
$\Omega_0$	Natural frequency
$\chi$	Resting state adjustment parameter
$r$	Ion concentration change rate
$\Delta I$	Feedback potential
$a_n$	General term formula of fully misaligned arrangement
$P_n$	Probability of fully misaligned arrangement
$P_l$	Probability of resting potential preconditions
$\bar{P}_n$	Average Probability of a single ion channel being blocked
$e$	Natural base

**Table B2.** Physical or physiological meaning of mathematical symbol used in mechanical pump model.

Mathematical symbol	Physical/Physiological meaning
$r_0$	Initial radius of ventricle in natural state
$r_-$	End systolic ventricular radius
$r_+$	End diastolic ventricular radius
$t_0$	Initial thickness of ventricular wall in natural state
$P_d$	Diastolic blood pressure of aorta
$P_s$	Systolic blood pressure of aorta
$\sigma_i$	Principal stress
$\varepsilon_x^+$	End diastolic circumferential strain
$\varepsilon_z^-$	End systolic radial strain
$E$	Elastic modulus
$\mu$	Poisson's ratio
$G$	Shear modulus
$\gamma$	Volumetric strain